Tectonophysics 936 (2026) 231299

Contents lists available at ScienceDirect

Tectonophysics

journal homepage: www.elsevier.com/locate/tecto

Emplacement mechanisms of the Córrego Seco post-collisional mafic pluton revealed by AMS and gravity data, Brasília Orogenic Belt

F.A. Temporim [a,b,*], G.S. Costa [a], G.F. Souza-Junior [c], R.P. Melo [d], L.M. Barros [a], S.W.O. Rodrigues [a], D.E. Cavalcanti [a], M.A. Reis [a], J.M.S. Carneiro [e], J.A.S. Fontoura [f], R.I.F. Trindade [c]

[a] Faculty of Science and Technology, Federal University of Goiás, Goiânia, GO 74971-451, Brazil
[b] Department of Geology, Federal University of Ouro Preto, Ouro Preto, MG 35402-163, Brazil
[c] Institute of Astronomy, Geophysics and Atmospheric Sciences, University of São Paulo, São Paulo, SP 05508-090, Brazil
[d] Department of Geology, São Paulo State University, Rio Claro, SP 13506-900, Brazil
[e] Serviço Geológico do Brasil, SGB, Goiânia, Goiás, Brazil
[f] Geoscience Institute, Federal University of Rio Grande do Sul, RS 91501-970, Brazil

ARTICLE INFO

Keywords:
Corrego Seco pluton
Anisotropy of magnetic Susceptibility
Gravity modeling
3D inversion
Brasília Orogenic Belt

ABSTRACT

The Córrego Seco (CS) pluton, located in the southern Brasília Orogenic Belt (BOB), central Brazil, represents a key expression of post-collisional mafic magmatism emplaced during the late Ediacaran (~630–610 Ma). The intrusion exhibits inverse zoning, with a gabbroic core surrounded by dioritic margins, and abundant mingling and hybridization textures that point to incremental construction by multiple magma pulses. To constrain its emplacement mechanisms, we integrate anisotropy of magnetic susceptibility (AMS), anisotropy of anhysteretic remanent magnetization (AARM), petrographic analyses, and gravity data. AMS and AARM fabrics reveal a concentric magnetic foliation pattern around the gabbroic core within a westward-dipping tabular pluton, reflecting magma flow and late-stage solid-state overprints. Petrographic observations highlight localized crystal-supported deformation along pluton margins and in adjacent country rocks, consistent with reduced melt fractions during final crystallization. Gravity modeling based on 73 new stations and 3D inversion demonstrates a westward-dipping geometry with thickened roots toward the west. These structural and geophysical features indicate that pluton emplacement was controlled by crustal-scale discontinuities and shear zones, with the asymmetric westward-dipping geometry being inconsistent with simple diapiric ballooning models. Integration of magnetic, petrographic, and gravimetric evidence supports a model of stepwise pluton assembly, where magma ascent was strongly controlled by inherited suture at the boundary between the Arenópolis Arc and the Anápolis–Itauçu Complex. This interpretation provides a key tectonic constraint, indicating that magmatism postdated the main suturing processes during the terminal stages of Gondwana amalgamation.

1. Introduction

Post-collisional mafic magmatism represents a key stage in the late evolution of orogenic systems, as it reflects the interaction between crustal thickening, lithospheric reworking, and mantle-derived inputs (Liègeois, 1998; Bonin, 2004; Patiño Douce, 1999; Wilson, 2012; Chiaradia, 2009). The ascent and emplacement of such magmas are commonly focused along inherited crustal discontinuities and deep regional shear zones, which act as preferential conduits for magma transfer through the crust (e.g. Marsh, 1982; Hutton, 1988; Bouchez et al., 1992; Archanjo et al., 2002; Solgadi and Sawyer, 2008; Martínez-Ardila et al., 2023). Recognizing the structural control on post-collisional intrusions is therefore fundamental for understanding how mafic magmas are emplaced within the orogenic crust, how they contribute to lithospheric reworking, and ultimately how they record the transition from collisional thickening to post-orogenic stabilization and, locally extension (Liègeois, 1998; Bonin, 2004; Paterson et al., 1999).

The Neoproterozoic amalgamation of West Gondwana produced the large (~1100 km long) Brasília Orogenic Belt (BOB) (e.g. Dias et al.,

* Corresponding author at: Faculty of Science and Technology, Federal University of Goiás, Goiânia, GO 74971-451, Brazil.
E-mail address: filipe.temporim@ufop.edu.br (F.A. Temporim).

https://doi.org/10.1016/j.tecto.2026.231299
Received 11 February 2026; Received in revised form 22 June 2026; Accepted 24 June 2026
Available online 3 July 2026

2025). BOB is part of a broader Neoproterozic-Early Paleozoic orogenic system in central Brazil (Almeida, 1968) that developed during amalgamation of three major paleocontinental blocks: the São Francisco, Amazon and Paranapamena (Dias et al., 2025). Driven by tectonic convergence, paleocontinental passive margins evolved into a complex accretionary system and subsequently into a collisional orogen (Dias et al., 2025). Throughout this evolution, intra-oceanic magmatic arcs accreted along the belt's western margin (Pimentel and Fuck, 1992; Pimentel et al., 2000a, 2000b), juxtaposing rocks with juvenile isotopic signatures (Pimentel and Fuck, 1992) and low-grade, forearc basin-related volcano-sedimentary successions (Laux et al., 2010) against the high-grade gneisses of the belt's metamorphic core (Lacerda Filho et al., 2021). Although available geophysical data are limited, these boundaries may delineate a first-order crustal discontinuity within the BOB.

As a result, the belt records a long-lived tectono-metamorphic and magmatic history culminating in the Ediacaran–Ordovician, marked by intense post-collisional magmatism (Piuzana et al., 2003). Plutons from the BOB are dated between 650 and 480 Ma (Piuzana et al., 2003; Silva et al., 2011; Lacerda Filho et al., 2021) and comprise two main episodes: (i) early post-collisional mafic–ultramafic intrusions emplaced between 650 and 590 Ma (Silva et al., 2011; Augustin and Della Giustina, 2019, Augustin et al., 2023; Carvalho et al., 2025), and (ii) late to post-collisional felsic intrusions between 550 and 480 Ma, dominated by metaluminous, high-K calc-alkaline to alkaline (A-type) granitoids (Pimentel et al., 1996; Pimentel, 2016). Aeromagnetic surveys (Silva et al., 2011) and detailed geological studies (Augustin and Della Giustina, 2019; Augustin et al., 2023) have delineated several of these bodies, revealing complex internal facies distributions.

The Córrego Seco Pluton (CS), focus of this study, intrudes arc-related rocks near the contact between the high-grade gneisses of the belt's metamorphic core and the accreted magmatic arc rocks. It displays an inverse composite zonation with mafic cores surrounded by dioritic to granodioritic margins and widespread mingling zones. Despite its relevance, few structural analyses have been carried out, and the CS is still commonly described as isotropic except for a foliation along its margins (Laux, 2004; Lacerda Filho et al., 2021). This makes it a key case for investigating how post-collisional mafic magmas were emplaced along crustal-scale structures during the late evolution of the BOB.

Among geophysical tools for constraining the subsurface geometry of intrusive bodies, gravity methods are particularly suitable, especially when combined with structural analyses (Améglio and Vigneresse, 1999). The integration of gravity modeling and anisotropy of magnetic susceptibility (AMS) provides robust insights into pluton architecture, since AMS records the last stages of magma movement before solidification while gravity constrains the three-dimensional geometry at depth (Vigneresse et al., 1999). This combined approach has been successfully applied to unravel pluton emplacement mechanisms in several orogenic settings (Aranguren et al., 1996; Améglio et al., 1997; Sant'Ovaia et al., 2000; Cruz et al., 2021; Souza Junior et al., 2021; Fontoura et al., 2024). Furthermore, recent tectonic syntheses emphasize that the terminal Ediacaran to Cambrian evolution of the BOB was governed by the interaction of strike-slip shear zones and localized extension within a thickened orogenic crust (e.g., Valeriano et al., 2008; Fuck et al., 2017), providing a broader framework for interpreting the emplacement of post-collisional mafic plutons.

In this paper, we integrate AMS, microstructural analysis, and new gravity data to investigate the emplacement of the Córrego Seco Pluton. Likely emplaced at mid-crustal levels, the CS provides a natural laboratory to evaluate how inherited crustal-scale shear zones guided magma ascent, incremental emplacement, and the development of asymmetric tabular pluton geometries during late- to post-collisional tectonism in the BOB.

2. Geological context

2.1. Regional context

The Brasília Orogenic Belt (BOB) is a ~ 1100 km belt developed along, the western margin of the São Francisco Craton (Almeida, 1967). It forms the eastern-central domain of the Tocantins Province (Almeida, 1968), which represents an orogenic system built during the Brasiliano-Pan-African orogenesis associated with West Gondwana amalgamation (Almeida et al., 1981) via convergence among the Paranapanema/Rio de la Plata Block, the Amazonian Craton, and the São Francisco Craton (Fig. 1A).

Between ca. ~900 and ~ 600 Ma, the BOB evolved from initial oceanic plate subduction and development of intra-oceanic magmatic arcs (Pimentel and Fuck, 1992; Laux et al., 2005; Cordani et al., 2013), through progressive terrane accretion during consumption of oceanic lithosphere (Pimentel, 2016) and the amalgamation of the Amazonian, Rio de la Plata/Paranapanema, and western Congo–São Francisco cratonic blocks (e.g., Cordani et al., 2003; Oriolo et al., 2017). This tectonic progression transformed an initially passive margin into a complex accretionary system and, ultimately, a collisional orogen (Pimentel, 2016). Convergence was accompanied by *syn*-collisional continental magmatism (Dias et al., 2025), followed by post-collisional relaxation with crustal extension and late to post-collisional magmatism (Piuzana et al., 2003; Augustin et al., 2023).

The BOB has an overall N—S orientation and an acurate geometry delineated by systematic changes in the dominant foliation: NE–SW in the Northern BOB and NW–SE in the Southern BOB (Fig. 1b) (Uhlein et al., 2012). Regionally, it is compartmentalized into five ~N-S-oriented tectonic zones (e.g., Fuck, 1994; Valeriano et al., 2008; Pimentel, 2016), arranged as follows; from east to west: (i) a foreland zone comprising Neoproterozoic, anchimetamorphic, shallow-marine sedimentary rocks organized in subhorizontal thrust sheets and underlying by cratonic basement rocks (Valeriano et al., 2008; Dias et al., 2025); (ii) an external allochthonous zone, represented by Neoproterozoic passive-margin shelf successions forming an imbricate thrust stack (Valeriano et al., 2008); (iii) an internal zone composed of metamorphic nappes that overlie the thrust-and-fold belt of the external zone to the east (Valeriano et al., 2008), and include high-grade rocks of the Anápolis–Itauçu Complex that constitutes the metamorphic core of the orogen (e.g. Pimentel, 2016; Dias et al., 2025); (iv) Goiás Massif, a probable allochtonous microcontinental block of Archean to Neoproterozoic crust (ca. 3.0–0.8 Ga; e.g., Cordeiro and de Oliveira, 2017); and (v) Goiás Magmatic Arc, consisting of metavolcano-sedimentary sequences and calc-alkaline orthogneisses ranging from gabbroic to granitic compositions, located in the westernmost part of the orogen (Pimentel and Fuck, 1992).

The Goiás Magmatic Arc is divided into two branches, separated by Archean-Paleoproterozoic rocks of the Goiás Massif (Pimentel, 2016; Fig. 1B). The northern branch comprises the Mara Rosa Arc (e.g., Pimentel et al., 1997; Viana et al., 1995), which encompasses metaplutonic rocks of tonalitic composition generated in two periods (ca. 900–800 Ma and ca. 700 to 600 Ma) separated by a narrow belt of supracrustal sequences (Cordeiro et al., 2021). The southern branch, the Arenópolis Arc (830–600 Ma), hosts the Córrego Seco intrusion studied here (Fig. 1B). It consists of six metavolcano-sedimentary sequences of distinct age, without a clear chronological gradient (Carneiro et al., 2021) exposed within dominant metaplutonic orthogneiss (Pimentel and Fuck, 1992), and affected by high-pressure collisional metamorphism recorded in the Anicuns–Itaberaí Sequence (Passo-Vieira et al., 2026).

The contact between the Arenópolis Arc and the internal zone of the BOB is characterized by a pronounced gravity gradient across the boundary and likely represents a crustal-scale discontinuity (Lacerda Filho et al., 2021). This boundary region hosts a suite of late to post-collisional mafic–ultramafic to intermediate–felsic intrusions,

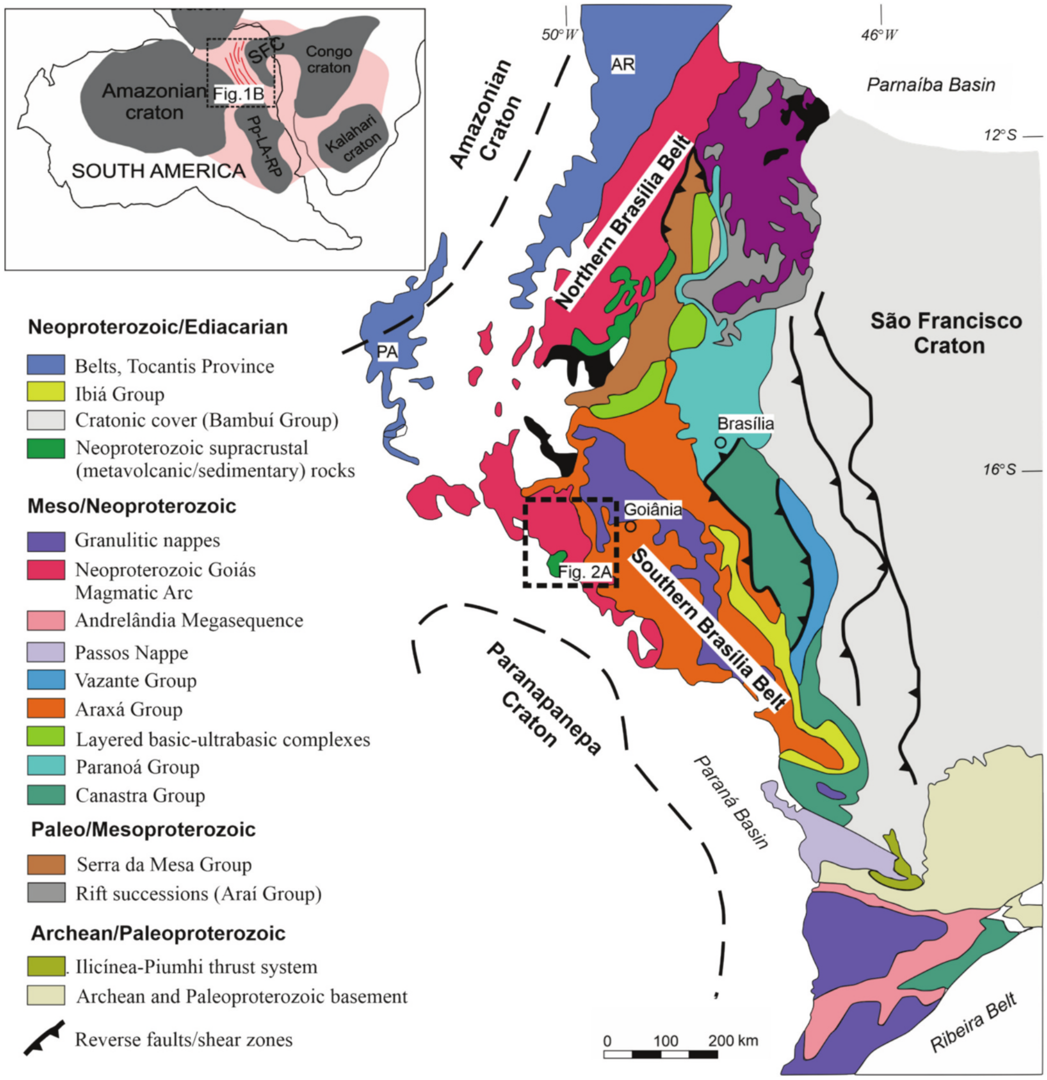

Fig. 1. Tectonic units of the Brasília Orogenic Belt (modified from Valeriano et al., 2008). A) Geographic representation of South America and Africa in a pre-drift configuration and the major geological cratons, built mainly based on Alkmim et al. (2006). Cratonic units in gray: Pp-La-Rp - Paranapanema, Luíz Alves, and Rio de la Plata craton, SFC - São Francisco Craton. Red lines represent structural lineaments from the BOB. The dotted square delimits the study area of Fig. 1B. B) Geological sketch map of the BOB (modified from Pimentel et al., 2000a, 2000b; Valeriano et al., 2008). The dotted square delimits the study area of the Córrego Seco Pluton and other post-collisional plutons represented in Fig. 2A. (For interpretation of the references to colour in this figure legend, the reader is referred to the web version of this article.)

including the Córrego Seco Pluton, and is defined by a major west-dipping structure (Fig. 1B; Lacerda Filho et al., 2021). Late to post-collisional magmatism occurred in two pulses: (i) ca. 650–590 Ma, dominated by mafic intrusions (including Córrego Seco) with minor felsic bodies (Mota and Silva, 2009; Silva et al., 2011; Augustin et al., 2023; Carvalho et al., 2025), and (ii) ca. 550–480 Ma, characterized chiefly by felsic magmatism. On aeromagnetic products from south-western Goiás, these late- to post-collisional mafic-ultramafic intrusions are readily recognized by their strong magnetic susceptibility contrast with the host rocks (Silva et al., 2011).

2.2. Structural control and geology of the Córrego Seco Pluton

The Córrego Seco Pluton intrudes orthogneiss and forearc-related volcano-sedimentary sequence of the Arenópolis Arc (Fig. 2A and 3A). Emplacement was located along the contact between these contrasting lithologies, coincident with a medium-angle ductile shear zone (with reverse senses) (Fig. 2B) developed between competent orthogneiss and ductile metavolcano-sedimentary rocks (Fig. 2B and 3C). This interpretation is supported by the occurrence of ductile deformation structures, such as mylonitic fabrics. The shear zone strikes N—S and records top-to-the-east transport (Fig. 2B). Metamorphic peak conditions estimated by Passo-Vieira et al. (2026) for this portion of the orogen reached approximately 660 °C and 1.16–1.30 GPa, corresponding to depths of ~38–48 km, consistent with mid- to lower-crustal conditions favorable for the development of ductile shear zones (Fossen and Cavalcante, 2017). Overall, the deformation pattern of the host terrane comprises a complex stack of tectonic slices involving metavolcano-sedimentary nappes and orthogneisses sheets (Fig. 2A). Folding within the volcano-sedimentary successions is evident in geological maps and cross-sections (e.g., Lacerda Filho et al., 2021), with axial traces predominantly NE–SW and N—S (Fig. 2C). The distribution of foliation measurements on geological maps and stereograms indicates a complex folding pattern affecting the volcano-sedimentary sequences and surrounding basement units. The main planar elements are gneissic layering (according to the concept of Wojtal et al., 2022) in orthogneiss and schistosity in metavolcano-sedimentary rocks. The gneissic layering is a planar fabric defined by compositional banding

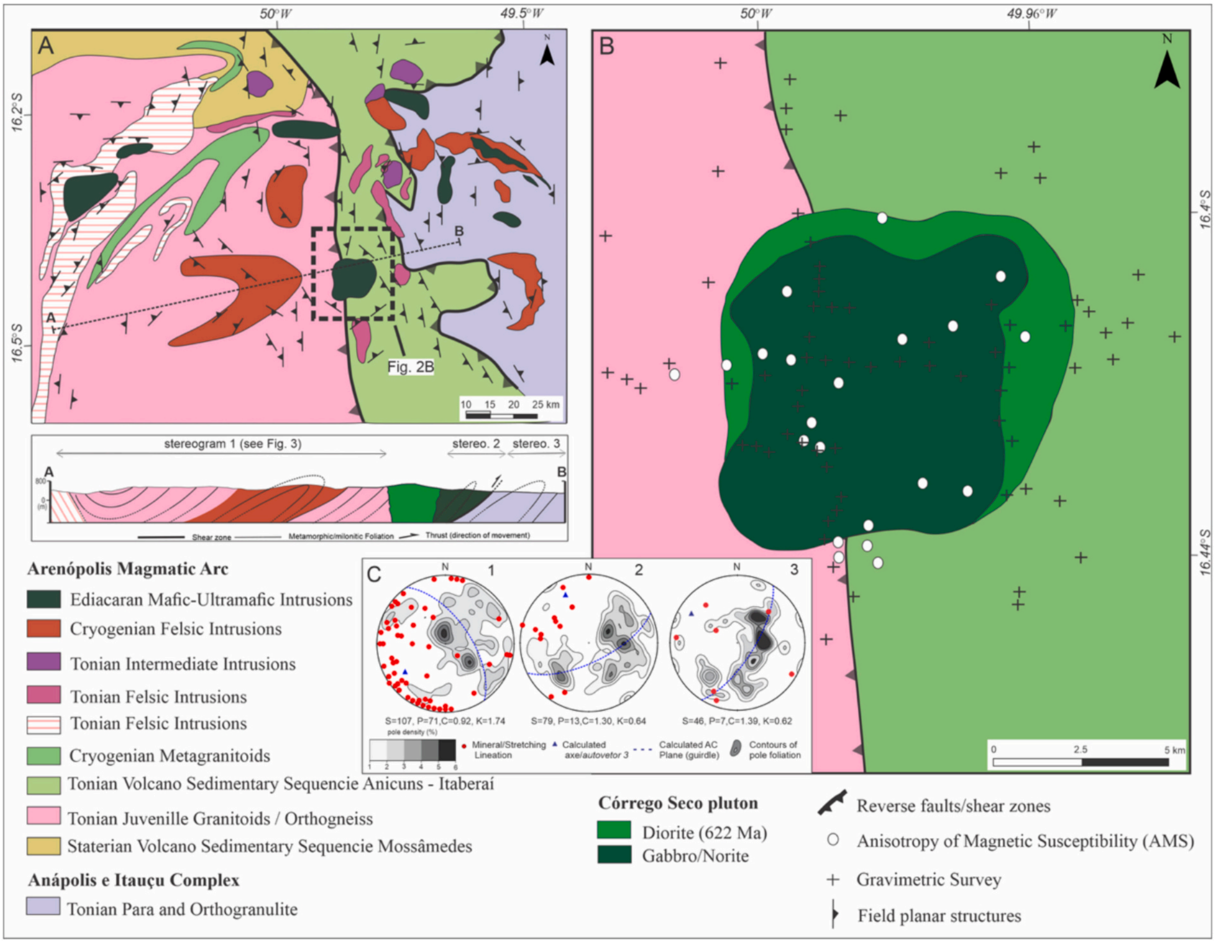

Fig. 2. (A) Geological map within the Arenópolis magmatic arc. The dotted square delimits the study area of the Córrego Seco Pluton. The reverse fault represents the contact between the Arenópolis Magmatic Arc and the inner BOB zone. (B) Geological map with the shape and facies distribution from Córrego Seco Pluton and the country rocks (modified from Lacerda Filho et al., 2021). Including AMS sampling sites (o) and our gravity stations (+) (C) Stereograms of the three recognized structural domains around the Córrego Seco Pluton.

with mineral alignment and stretching of quartz and feldspar. Schistosity is defined by the preferred orientation of micaceous minerals, together with quartz and feldspar, in the metavolcano-sedimentary units. Associated with the foliations are stretching lineations (in orthogneisses) and mineral lineations (in metavolcano-sedimentary rocks).

The stereograms in Fig. 2C summarize the structure of the three structural domains recognized around the Córrego Seco Pluton. These domains correspond to distinct lithostratigraphic units separated by major tectonic boundaries: (Améglio and Vigneresse, 1999) an orthogneiss-dominated domain west of the pluton (stereogram 1); (Améglio et al., 1997) metavolcano-sedimentary rocks of the Anicuns–Itaberaí Sequence (stereogram 2); and (Almeida, 1968) orthogranulitic rocks of the Anápolis–Itauçu Complex (stereogram 3), to the east.

The C index (Woodcock, 1977) expresses the dispersion of the sample, tending to infinity when there is a strong preferred orientation, and approaching zero when the distribution is random. The K index (Woodcock, 1977) refers to the shape of the distribution: higher values indicate clustering, whereas lower values reflect girdle distributions on stereograms. The foliations display strong dispersion, with C values between 0.92 and 1.39, suggesting high variability. K values range from 0.62 to 1.74, indicating data distributions that transition between girdle and unimodal patterns. Isofrequency contour curves in the stereograms show girdle distributions, especially in stereogram 3, with girdle oriented differently in each structural domain. In domains 2 and 3, however, the girdle trend NE–SW, with eigenvector 3 (calculated axis) in the NW quadrant, parallel to certain stretching lineation concentrations.

The contrasting isofrequency patterns between structural domains suggest allochthony among the lithostratigraphic units surrounding the Córrego Seco Pluton. Stretching/mineral lineations (Fig. 3B) also show variable orientations and strong dispersion across the domains. In general, the stereograms highlight folds with NW–SE axial planes, consistent with those observed in maps and profiles. These folds are asymmetric, with tight to isoclinal interlimb angles and inclined axial planes and axes. The C and K indices indicate that these structures do not represent ideal cylindrical folds, or that subsequent folding/deformation phases modified the original pattern.

The Córrego Seco (CS) pluton, first named by Nunes (1990) and later mapped by Araújo et al. (1997), covers ~40 km^2 and is elliptical to near circular, with concentric internal structures. Although intrusive contacts are not frequently exposed, due to thick soil cover, the geometry of the pluton is constrained by aerogeophysical data (Silva et al., 2011).

The CS pluton is inversely zoned, with dioritic rocks at the margins grading inward to mafic core. The core of the intrusion is dominated by hornblende gabbro, hornblende grabro-norite and hornblende norite (Laux et al., 2005). These mafic rocks are predominantly melanocratic, dark gray to greenish, apparently isotropic at mesoscopic scale (Fig. 3F), with fine to coarse granoblastic texture and mineral assemblages of pyroxene, plagioclase and hornblende. Toward the margins, diorites and quartz diorites are dominant (Lacerda Filho et al., 2021). The border zone preserves clear evidence of mingling between contrasting magmas, producing enclave swarms with variable degrees of hybridization within

Fig. 3. Pictures of the Córrego Seco Pluton, (a) thrust fault separating the metasedimentary sequence of the Anicuns–Itaberaí Group (to the east) from the orthogranulitic rocks of the Anápolis–Itauçu Complex (to the west). A sigmoidal vein highlights top-to-the-east transport, (b) mineral lineation related to the same shear zone structure, (c) refolding pattern within metasedimentary units, (d) igneous flow fabric defined by aligned feldspars, (e) Mingling of two magmas with contrasting physical properties, forming large mingled zones of enclave swarms in different degrees of hybridization with the granite, (f) sample of gabbro from the pluton core, displaying coarse-grained texture.

the diorite, consistent with coeval magmatic interaction (Fig. 3D,F).

Geochronological constraints for CS remain sparse. U—Pb zircon ages for the dioritic facies of 623 ± 13 Ma (Laux et al., 2005) and 622 ± 6 Ma (Nunes, 1990) establish the emplacement in the late Neoproterozoic. Initial εNd(T) values between +1.8 and + 2.6 (Laux et al., 2005), indicate magma origin from a depleted mantle source, with limited crustal contamination.

2.3. Microscopic features

A magmatic structure deformation origin is recognized for foliations defined by the alignment of igneous, commonly euhedral minerals, particularly where the foliation is parallel to internal or external pluton contacts (Bouchez et al., 1981; Nédélec and Bouchez, 2015, Bouchez and Nicolas, 2021). Foliations formed during expansion or 'ballooning' of diapirs may be strictly magmatic in origin, although some studies suggest that solid-state deformation also may occur (Paterson et al., 1989; Molyneux and Hutton, 2000). In this sense, deformation in crystal–melt systems refers to the mechanical interaction among crystals within interstitial melt, producing magmatic flow fabrics that reflect the relative movement of a partially crystallized mush. By contrast, intracrystalline deformation of igneous minerals provides direct evidence of high-temperature solid-state deformation, commonly developed when crystal-rich magmas approach the final stages of crystallization (e.g., Cavalcante et al., 2021; Nédélec and Bouchez, 2015). Otherwise, a strictly tectonic origin for foliations in magmatic rocks is favored when the foliation is defined by metamorphic minerals, no alignment of igneous minerals occurs, the foliation is locally at high angles to pluton and country rocks contacts, and the foliation is continuous with a regionally developed cleavage (Paterson et al., 1989).

Overgrowth textures refer to those mineral phases formed on the crystal faces of an already crystallized mineral. Chemical zoning can be described as evidence of different compositions in distinct growth sectors of a single mineral (Dowty, 1976). These zones form during cooling through a continuous chemical reaction between the mineral and the liquid. The poikilitic overgrowth microtexture is characterized by small granular crystals randomly enclosed within a larger crystal of another mineral (Philpotts, 1990). The smaller crystals, known as chadacrysts, preserve their shape (euhedral/subhedral). Meanwhile, the larger crystals, called the oikocrysts, do not have well-developed crystal faces and appear to have crystallized after the chadacrysts (Philpotts, 1990). Poikilitic texture with tabular biotite chadacrysts enclosed by plagioclase oikocryst (Fig. 4A) and overgrowth in zoned euhedral plagioclase (Fig. 4B) are present and represent unequivocal magmatic growth features.

Microscopic features allow us to distinguish magmatic and solid-state deformation microstructures using widely used criteria (Bouchez et al., 1981; Passchier and Trouw, 2006, Vernon, 2018, Nédélec and Bouchez, 2015among others). Evidence of quartz-feldspathic residual melt is suggested by magmatic features including microfractures and embayments in deformed feldspars, which are filled by a fine-grained of quartz and/or plagioclase (Fig. 4C). Limited intracrystalline plasticity is indicated by deformation twins (Fig.s 4B–E), microkinks (Fig. 4D), and undulose extinction (Fig. 4E) in plagioclase. Solid-state deformation is indicated by polycrystalline feldspar with irregular grain boundaries formed in response to bulging (BLG) recrystallization (Fig. 4D,E,F).

3. Methods

3.1. Magnetic analysis

Oriented samples were extracted from 28 sites spaced at ~1 km, evenly distributed across the pluton (Fig. 2B) except for some areas of difficult access. Between seven and ten cores of approximately 8 cm in length and 2.5 cm in diameter were collected at each site using a portable gasoline-powered drill. The cores were oriented in situ with both magnetic and solar compasses. In the laboratory, each core was cut into standard specimens that were 2.2 cm in length providing a total of 258 specimens. All measurements were performed at the Laboratório de Paleomagnetismo e Magnetismo de Rochas (USPmag) of the Instituto de Astronomia, Geofísica e Ciências Atmosféricas of the Universidade de São Paulo (IAG-USP).

The anisotropy of magnetic susceptibility (AMS) provides a semi-quantitative fabric description of magmatic rocks (Bouchez, 1997). The AMS is second-rank symmetrical tensor, but it is commonly represented as an ellipsoid with three orthogonal axes ($k_1 > k_2 > k_3$). The parameter P is defined as the degree of anisotropy, $P = k_1/k_3$ with $P = 1$ corresponding to a fully isotropic sample. The parameter T is defined as the shape factor, $T = 2\ln(k_2/k3)/\ln(k_1/k_3) - 1$, reflecting the shape of the AMS ellipsoid and varying from +1 for oblate, purely planar magnetic

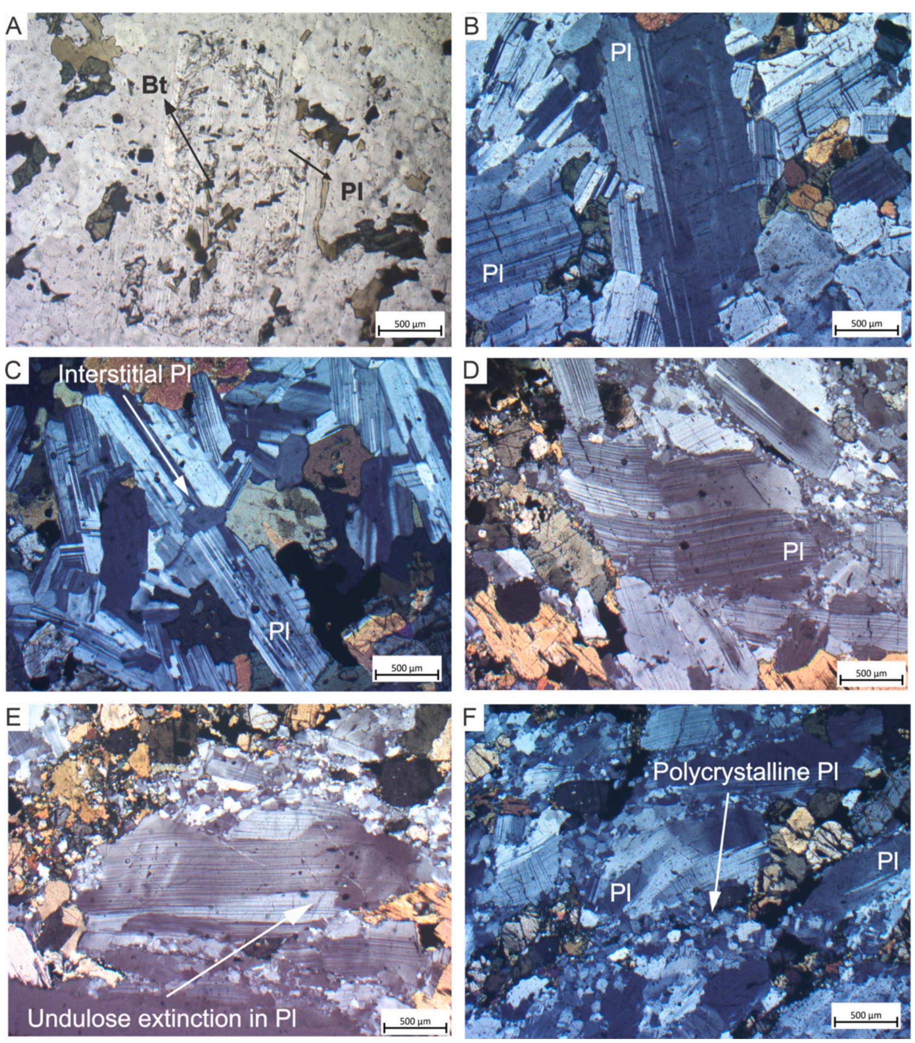

Fig. 4. Images of microtextures and microstructures of the Corrego Seco Pluton: (a) Poikilitic texture with tabular biotite chadacrysts enclosed by a plagioclase oikocryst, in twinned feldspar crystals with tapering edges, (b) chemical zonation in euhedral plagioclase, (c) microfractures and embayments in deformed feldspars filled by a fine-grained of quartz and/or plagioclase, (d) deformed twins in plagioclase, (e) undulose extinction in plagioclase and deformed twins in plagioclase, (f) polycrystalline feldspar with irregular grain boundaries formed in response to bulging (BLG) recrystallization.

fabric (i.e. $k_1 = k_2 >> k_3$) through 0 (neutral) to −1 for prolate, purely linear magnetic fabric (i.e. $k_1 >> k_2 = k3$). The AMS of individual samples was measured using an Agico Kappabridge MFK 1 A. The software used was Anisoft6 and the statistical evaluation of the magnetic anisotropy in individual sites was obtained using the methods of Jelínek (1978) implemented in the ANISOFT program package (Hrouda et al., 1990). The AMS directional data were filtered to discard sites with high internal dispersion (ε12, ε 23) greater >26.5° (Jelínek, 1978). The anhysteretic anisotropy of remanent magnetization (AARM) reflects the sole ferromagnetic (*lato* sensu) contribution in the mineral fabric. To further restrict the selection of fabric carriers, we obtained the AARM within a coercivity window between 0 and 50 mT along 12 different orientations. A total of 4 (four) sites were selected according to their representability in each geological unit in the CS.

To explore the contribution of specific minerals to the bulk rock magnetic susceptibility, thermomagnetic experiments were carried out on the same four sites where AARM was applied. To accomplish that, the samples were crushed into a powder using an agate mortar, followed by measurement acquisition utilizing the Agico Kappabride KLY 4 CS, during both low and high-temperature cycles. Low-temperature curves were executed applying liquid nitrogen until the sample reached -195 °C. High-temperatures experiments were performed under a constant flow argon atmosphere to avoid excessive oxidation. In both high- and low-temperature experiments, we subtracted the signal of the sample holder along with the respective apparatus: the furnace for the high-temperature curve and the crystal for the low-temperature curve. Hysteresis curves were obtained with a vibrating sample magnetometer (VSM) MicroMag 3900 (Princeton Measurements Corp).

3.2. Magnetic mineralogy

Magnetic susceptibility versus temperature (K-T) curves were analyzed for four samples from each lithology of the CS pluton in order to identify the ferromagnetic minerals. The SI11 and SI20 sites represent the diorite, and the SI13 and SI24 samples represent the gabbro (Fig. 5). Specimens from CS pluton show similar, simple behaviors during cooling and heating. The K–T curves of all samples exhibit major transitions, identified from the derivative of the curves (dK/dT), near the Verwey Transition of magnetite (VT; approximately −180 °C) and the Curie temperature of magnetite (MCT; approximately 580 °C), manifesting the dominance of this mineral over the whole magnetic fabric. Still the samples SI20, SI13 and SI24 curves kept a sluggish decay, exceeding the Néel temperature of hematite (680 °C), which is an indication of its presence.

For sample SI11, a subtle hump is observed in the heating curve, which may correspond to maghemite that is destroyed during heating and, therefore, does not reappear upon cooling. The samples SI20 and SI24 show a distinct increase in susceptibility during cooling, which is likely related to oxidation processes during heating, producing Ti-poor magnetite. In contrast, sample SI13 presents a reversible curve, with only a slight Hopkinson peak at low temperatures, suggesting the presence of single-domain (SD) magnetite.

The hysteresis loops were applied to investigate the magnetic domain states of the lithotypes present in the CS and were obtained with a vibrating sample magnetometer (VSM) MicroMag 3900 (Princeton Measurements Corp). All the analyzed samples reflect hysteresis loops with lower coercivity and are classified as multi-domain (MD), as the Mrs./Ms. and Hcr/Hc ratios fall within the MD spectrum on the Dayplot (Day et al., 1977).

3.3. Anisotropy of magnetic susceptibility

Table 1 summarizes the results of the site mean principal susceptibility axis (K_1, K_2 and K_3) and their associated errors, and parameters (T, P and Km) of the measured AMS. The filtering process excluded very few data, with only magnetic lineations showing low dispersion at the site level 96%. Each station is characterized by the mean anisotropy parameters of a minimum of seven specimens. For the gabbroic compositions, K_m ranges from 2.856×10^{-3} to 132.1×10^{-3}. For dioritic compositions, K_m ranges from 1.373×10^{-3} to 48.31×10^{-3}. No CS K_m data is $<10^{-3}$, which according to Rochette (1987) might be a ferromagnetic rock behavior caused by ferromagnetic minerals such as magnetite, supported by magnetic mineralogy (see in topic 3.2). The values of k vary widely according to different parts of the pluton. This spatial variability of K determines that there is no relationship between a lithotype inside the CS. The values of T and P vary widely according to different parts of the pluton. The highest values are located in the northern portion of the pluton, while the lowest values are located in the southern portion. For dioritic compositions, P ranges from 1.089 to 1.332, and most ellipsoids are oblate in shape. For the gabbroic compositions, P ranges from 1.029 to 1.400, and most ellipsoids are oblate in shape. For country rocks, P ranges from 1.041 to 1.245, and the oblate magnetic fabrics are slightly more abundant than the prolate variety. We depict all magnetic foliation and lineation data after filtering out sites with low internal coherence (Fig. 6). Magnetic foliation and lineation from all lithotypes exhibit a distinct concentric pattern surrounding the mafic core. The border of the CS exhibits a concentric structure through both magnetic lineation and foliation. The lineation (K1) is predominantly characterized by low angles, with few data points at high angles. K_3 exhibits a similar structuring to K_1, characterized by foliation plane with low plunge angles. The inner zone of the CS presents a clear concentric distribution, with K_1 and K_3 varying from low to high plunge angles.

The AMS and AARM results for the CS pluton exhibited similarities (Fig. 7). Magnetic fabrics obtained from both techniques were consistent across all samples, suggesting a predominant influence of MD magnetite in defining the magnetic fabric within the pluton. This similarity indicates that any dispersion observed in the AMS fabric is likely due to variations in the orientation of MD magnetite grains rather than the presence of other magnetic phases.

4. Gravity data acquisition

For this study, the gravity dataset consists of 73 new gravity stations collected during fieldwork in 2023 (Fig. 2B). Data acquisition was performed using a CG-5 Autograv gravimeter, with a precision of ±0.01 mGal, while orthometric altitudes, referenced to the WGS84 ellipsoid, were measured with Differential Global Positioning System (DGPS) equipment (±0.3 m). Station spacing was approximately 500 m along three profiles crossing the CS, with two in the N-S direction and one in the *E*-W direction. In the country rocks, station spacing increased to around 800 m.

4.1. Data processing

The gravity network is referenced to an altimetric base from the Brazilian Institute of Geography and Statistics (IBGE), located at 16°30′19.58" S, 50°03′51.28" W. Tidal and instrument drift corrections were applied using the software Oasis Montaj (Geosoft Inc, 2015), while the remaining processing steps followed a different approach to compute the Bouguer disturbance.

Orthometric altitudes (H) were converted from both the newly acquired gravimetric dataset and the topographic database (30 m × 30 m resolution). The geoid height (N) for the study area was extracted from the GMT database (Wessel et al., 2019), which provides an approximate resolution of 10 km × 10 km. To ensure consistency with the gravity dataset, the geoid height values were interpolated using the nearest neighbor method in the Verde Python library (Uieda, 2018) to match the resolution of the orthometric topography. The geometric altitude (h = H + N) was then computed, ensuring that all altitude values were referenced to the WGS84 ellipsoid (Zone 22S).

The normal gravity field (g) was calculated using the theoretical

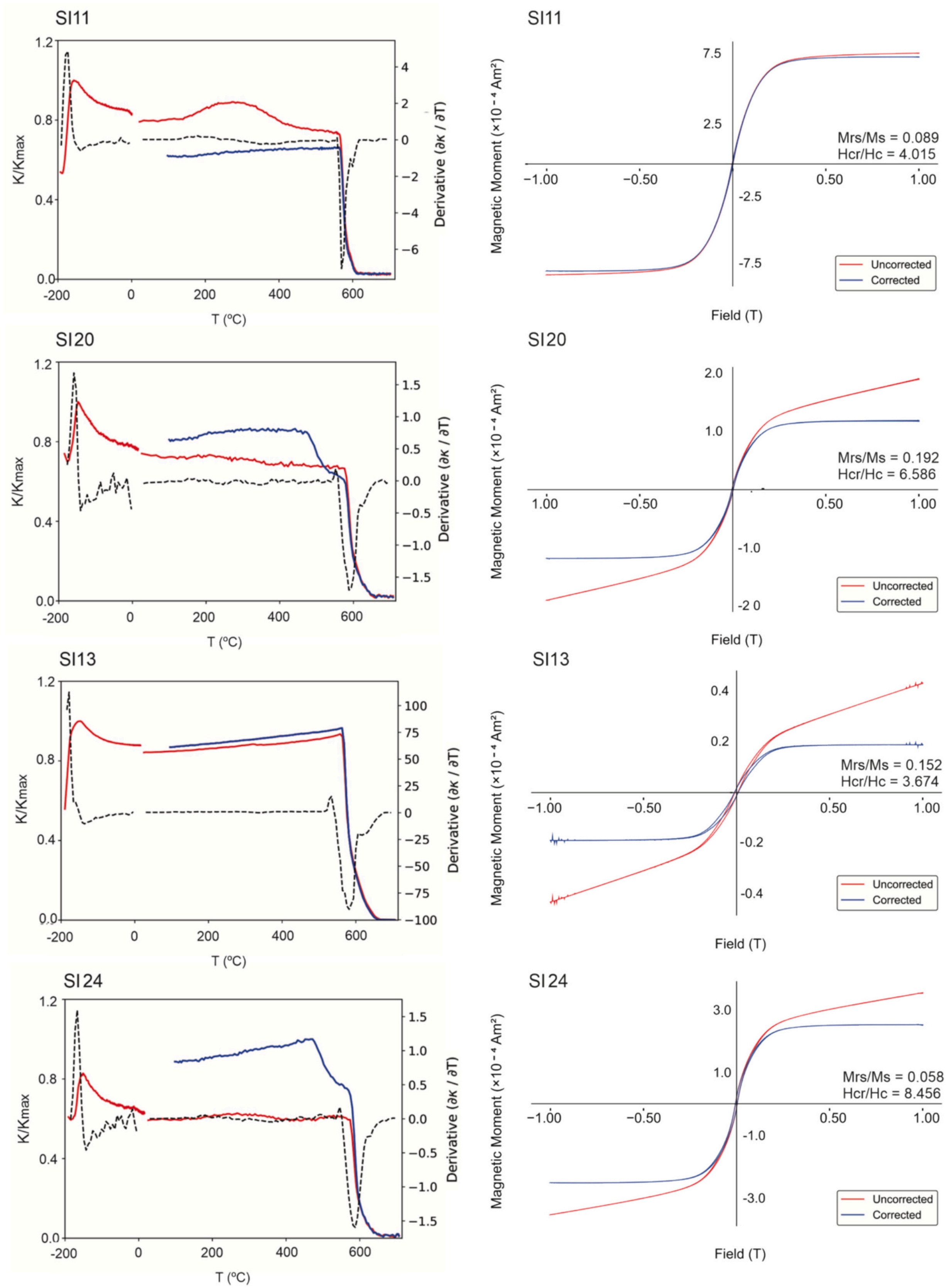

Fig. 5. Representative thermomagnetic curves for four samples of the Córrego Seco Pluton. The y-axis is the bulk of magnetic susceptibility and the x-axis is the temperature in degrees Celsius. The red lines represent the heating, blue lines represent the cooling, and the black dashed lines are the first derivative ($\partial k/\partial T$). In the hysteresis curves for the same sites, the magnetic moment was normalized by the mass. (For interpretation of the references to colour in this figure legend, the reader is referred to the web version of this article.)

Table 1
Anisotropy of magnetic susceptibility parameters of the Córrego Seco pluton. Site number; number of specimens measured (N); longitude, latitude – geographical coordinates; Km = mean magnetic susceptibility (10^{-3}SI); P = degree of anisotropy of the magnetic susceptibility ($P = k1/k_3$); T = AMS ellipsoid shape parameter [$T = 2\ln(k_2/k_3) / \ln(k_1/k_3) - 1$]; K_1 = trend and plunge of magnetic lineation (in degrees); K_2 = trend and plunge of the intermediate anisotropy axis; K_3 = trend and plunge of the pole of the magnetic foliation; ε_{12}, ε_{23}, ε_{31} are the semi-angle (measured in degrees) of confidence ellipses of AMS axes from Jelínek's (1978) statistics.

Site (n)	N	Location		Scalar data			Direction of principal axes					
		Geographical coordinates		K_m ($10^{-3}SI$)	P	T	k_1	ε_{12} (k_1)	k_2	ε_{23} (k_2)	k_3	ε_{31} (k_3)
Diorite												
SI1	7	49° 59′ 5.981″	16° 23′ 34.780″	48.31	1.332	0.085	255/ 97	13.9/8.2	137/40	17.7/8.4	009/36	19.8/6.7
SI11	8	60° 0′ 56.526″	16° 24′ 53.142″	2.409	1.219	0.130	94/38	7.3/5.7	239/47	9.6/6.5	349/18	9.9/5.1
SI14	7	49° 57′ 49.489″	16° 24′ 33.011″	37.88	1.220	0.215	250/10	5.8/1.8	160/3	7.1/1.3	54/79	5.1/1.7
SI20	9	49° 59′ 6.409″	16° 23′ 30.292″	7.172	1.220	0.153	102/4.5	12.9/7.9	009/34	15.8/7.7	198/56	12.9/6.5
SI21	7	50° 0′ 27.116″	16° 24′ 46.718″	1.373	1.099	0.536	203/16	18.8/2.8	110/10	20.9/8.2	348/71	12.9/3.1
SI22	8	50° 0′ 9.416″	16° 24′ 42.344″	6.121	1.087	−0.061	241/8	6.8/3.4	149/17	9.6/6.5	355/71	9.5/3.1
Gabbro/Norite												
SI3	10	49° 58′ 12.465″	16° 24′ 55.284″	5.874	1.109	0.138	248/26	21.1/2.4	169/41	24.3/4.9	37/38	14.2/2.4
SI4	10	49° 58′ 48.148″	16° 25′ 12.021″	2.971	1.120	0.396	156/34	13.2/4.3	267/28	15.6/9.9	27/43	13.1/4.1
SI5	10	49° 59′ 51.065″	16° 25′ 30.513″	2.856	1.110	0.246	99/25	22.8/7	195/11	24.4/11	307/61	16.4/8.9
SI6	10	49° 59′ 35.788″	16° 25′ 24.811″	4.973	1.139	0.723	24/45	38/3	288/6	38/6.5	192/44	7.5/3.3
SI7	11	50° 40′ 38.592″	16° 22′ 18.800″	87.75	1.106	0.189	105/54	12.4/7.8	11/3	12.8/5	279/36	14.4/6
SI8	12	49° 59′ 7.366″	16° 26′ 29.819″	15.84	1.298	−0.365	78/27	6.6/6.5	226/59	5/2.7	341/14	5.7/2.9
SI12	7	49° 58′ 43.674″	16° 25′ 48.704″	14.98	1.140	0.466	149/14	17.1/7.6	288/72	17.4/8.9	56/12	11.9/4
SI13	10	49° 58′ 19.411″	16° 25′ 52.815″	132.1	1.122	−0.113	214/31	16.2/9.7	120/6	12.1/9.3	21/59	15.7/8.6
SI15	8	49° 59′ 2.364″	16° 24′ 1.706″	81.98	1.201	0.652	28/76	9.8/6.2	265/8	10/4.7	173/12	10/5.5
SI16	10	49° 58′ 27.780″	16° 24′ 27.830″	71.4	1.150	0.382	34/3	5.4/2	126/26	5.1/2	297/64	3.8/1.8
SI17	10	49° 58′ 55.086″	16° 24′ 34.503″	81	1.400	0.68	45/14	20.4/2.7	137/6	20.4/2.3	250/45	4/1.9
SI18	11	49° 59′ 54.196″	16° 24′ 45.298″	49.43	1.184	0.741	296/62	14.4/3.8	175/16	15.5/7.3	77/22	10.4/2.2
SI19	9	49° 59′ 56.399″	16° 24′ 10.035″	70.95	1.243	0.242	65/37	10.5/3	333/3	15.4/5.6	239/52	12.9/2.4
SI23	9	49° 59′ 47.273″	16° 25′ 26.981″	118.2	1.100	0.117	285/51	17.9/6.6	109/38	15.9/7.4	17/2	22.4/4.7
SI24	10	49° 59′ 38.626″	16° 25′ 30.194″	2.835	1.174	0.05	96/1	8.8/2	189/66	14.3/6.7	6/24	14.4/5.6
SI26	7	49° 59′ 12.185″	16° 26′ 10.741″	7.948	1.229	0.108	295/3	12.3/1.4	1/64	13.1/1.2	173/26	8.5/2.4
SI28	10	49° 59′ 28.817″	16° 24′ 57.118″	2.974	1.079	−0.139	69/44	18.5/10.1	213/39	23.1/17.8	319/19	22.8/10
Country Rocks												
SI2	9	50° 0′ 20.359″	16° 24′ 58.210″	162.4	1.208	0.619	311/7	23/10.5	217/27	20.6/15.6	54/62	17.9/13.1
SI10	7	49° 59′ 28.629″	16° 26′ 19.281″	1.233	1.044	0.398	86/12	15.8/4.9	182/24	11.1/3.9	331/62	12.7/4.3
SI25	7	49° 59′ 12.806″	16° 26′ 20.994″	85.09	1.027	0.374	42/44	24.8/6.6	229/46	24.6/4.6	135/3	8/3.7
SI27	10	49° 59′ 28.151″	16° 26′ 26.990″	133.3	1.110	−0.075	296/56	14.7/7.9	67/24	20.7/8.9	168/23	18.6/8.1

formulation for the WGS84 ellipsoid, providing expected gravity values at each station through the Boule package (Uieda and Soler, 2020a), which implements the closed-form formula of Li and Götze (2001) to compute the normal gravity given latitude and geometric height of each station. The normal gravity represents the magnitude of the gradient of the gravity potential generated by a rotational bi-axial ellipsoid with the same mass, angular velocity, and surface potential as the geoid (Pašteka et al., 2017). Since this theoretical gravity formulation requires geometric heights, the conversion of orthometric altitudes to geometric heights was necessary in the first step to ensure consistency within this reference frame.

Once the normal gravity was obtained, the effect of the topography was removed, which is not accounted for in the theoretical gravity model (Gupta, 2021). Instead of applying the traditional infinite slab Bouguer correction — which assumes a homogeneous slab of thickness equal to the orthometric height (Lowrie, 1997) — we opted for a more accurate approach based on forward modeling (Nagy et al., 2000). This method is particularly relevant given that the study area presents sharp topographic variations, which could introduce significant errors when using the infinite slab approximation. To model the topographic effect, the terrain was discretized into rectangular prisms of 30 m × 30 m × h m, assuming a uniform density of ρ = 2690 kg/mˆ3 (Table S1), representative of the average density of the country rock lithology. The gravitational effect of each prism was then computed using a forward model to obtain the total topographic correction, which was subtracted from the observed gravity values, along with the normal gravity, to compute the Bouguer disturbance (Fig. 8A).

The Bouguer disturbance results from the lateral density contrasts between the rocks in the subsurface (Améglio et al., 1997). Since potential fields are additive, they comprise long-wavelength components associated with deep density variations (regional anomalies) and short-wavelength components linked to shallow mass distributions (residual anomalies) (Telford et al., 1990; Lowrie, 1997). For studies involving smaller-scale bodies, it becomes necessary to apply the regional-residual separation method. However, since the field dataset alone did not provide sufficient regional coverage for an accurate regional correction, we complemented the dataset with satellite-derived gravity data from the EGM2008 model, obtained from the ICGEM database (Ince et al., 2019) as a regular grid. We followed the same processing steps described earlier for the satellite-derived data to obtain the Bouguer disturbance, except for the density of the topography, which we assumed was the crust's average density of 2670 kg/m^3 (Hinze, 2003). To estimate the regional gravity field, we applied the deep equivalent layer (Dampney, 1969) directly to the Bouguer disturbance derived from the satellite gravity data. This 30 km-deep equivalent layer was fitted to extract only the long-wavelength components of the gravity field. The resulting regional anomaly was interpolated at the field measurement locations (Fig. 8B) using the nearest neighbor method in the Verde Python library (Uieda, 2018).

The residual gravity anomaly was obtained by subtracting the regional anomaly from the Bouguer disturbance (Fig. 8C). This residual anomaly was then interpolated onto a regular grid using a shallow equivalent layer (2.5 km), producing the final gravity anomaly map at a constant height of 1000 m (Fig. 9A). The technique can be used to predict the values for the gravimetric and magnetic field at any point, such as regular grids and different heights, while also outperforming other 2D interpolators like the minimum curvature or bi-harmonic splines (Soler and Uieda, 2020; Uieda and Soler, 2020b).

4.2. Gravity modeling

The tridimensional inversion was conducted using the SimPEG software (Cockett et al., 2015), using a residual gravity grid (Fig. 9A) and a topographic grid as input data. The a priori information used in the

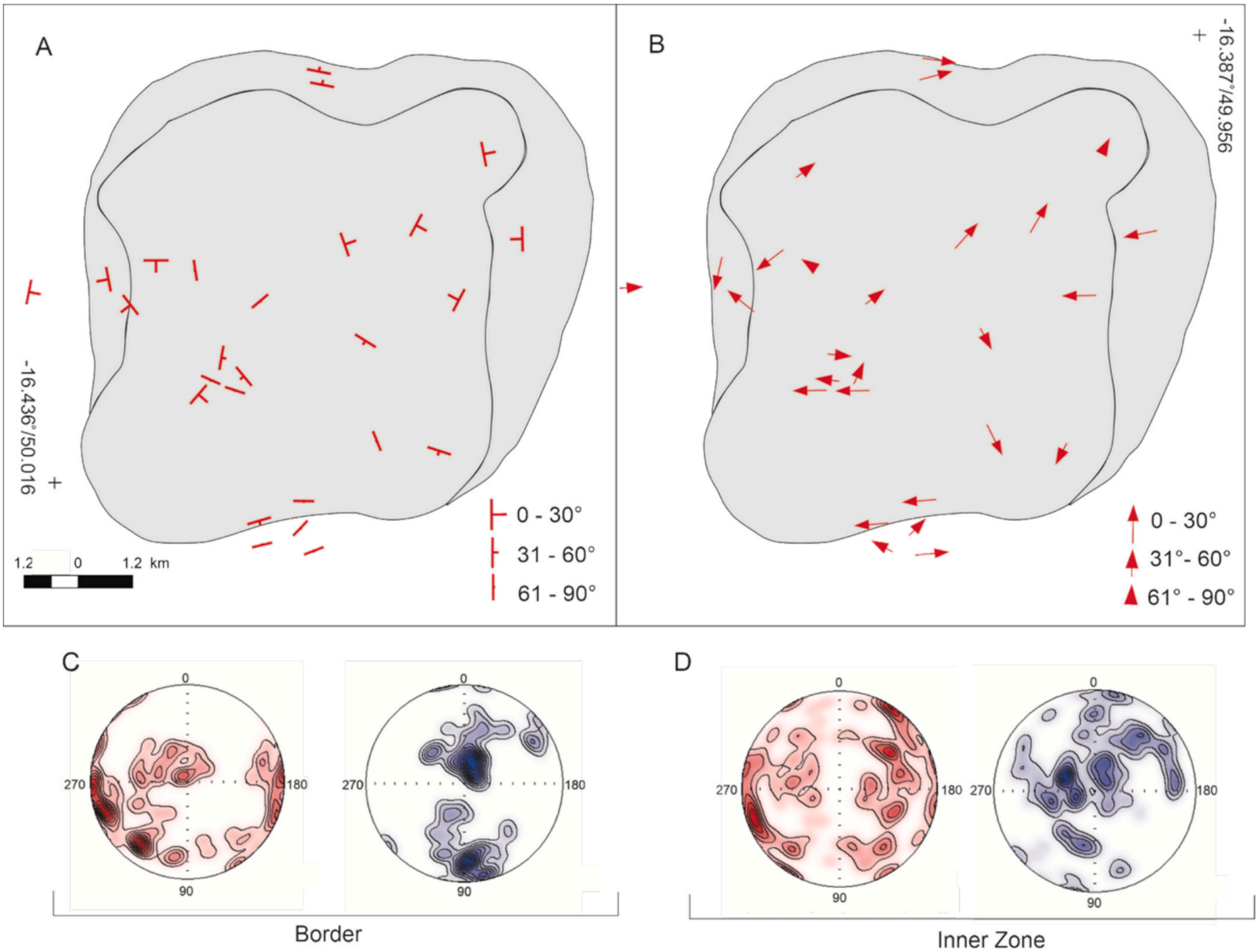

Fig. 6. AMS directional data after elimination of scattered sites (for error ellipses above 26°). (a) Magnetic foliations (k3); (b) magnetic lineations (k_1); contour plot of Kmax (red) and Kmin (blue) on the (c) border, and (d) inner zone of the pluton. (For interpretation of the references to colour in this figure legend, the reader is referred to the web version of this article.)

modeling was obtained from two main sources. The first was the shapefile of the pluton, which provided information on the regions where it outcrops. The second source came from borehole data used in the rock magnetism study. To achieve higher precision in density determination, we used the buoyancy method, measuring the sample's dry weight and the buoyant force acting on it while suspend by a negligible-mass thread in deionized water (Table S1). The results yielded an average density of 2920 ± 70 kg/m^3 ($n = 70$) for gabbro, 2850 ± 50 kg/m^3 ($n = 40$) for diorite, and 2690 ± 100 kg/m^3 ($n = 53$) for the surrounding country rock (see geologic map Fig. 2B).

The study area was discretized into a mesh with a minimum cell size of 500 m in all directions (x, y, and z). The mesh was horizontally centered at the plutonic body's centroid and vertically aligned with the highest topographic elevation. The resolution in the central region is refined with the minimum cell size near the body and progressively increased in cell size as it extends outward. Then, the active cells were defined, which excluded regions above the topographic surface from the inversion domain to optimize computation and results. These cells represent air and do not contribute to the gravity signal.

To further improve model accuracy, the first layer of cells in the outcropping central region of the plutonic body was assigned a positive density contrast of +230 kg/m^3. This value corresponds to the average contrast density of the gabbroic rock exposed in the area (Supplementary Table S1). This assignment served as a reference model, and a smallness regularization parameter ($\alpha_s = 2$) was employed to penalize deviations from this density, which enforces strong adherence to the reference model in regions where prior density values are available, preserving known geological constraints. Additionally, the directional smoothness regularization parameters ($\alpha_x = \alpha_y = \alpha_z = 1$) were implemented to promote smooth variations in all directions. This ensures continuity throughout the model while still allowing some discontinuities, such as the pluton boundaries. The choice of a reference model with values set to zero in the remaining mesh was due to the topographic correction applied using the average density of the country rocks. The inversion was performed using a weighting regularization based on distances, giving higher weights to regions closer to the surface since the body is exposed, which stopped upon meeting the SimPEG-defined tolerance criteria for changes in the objective function and model updates (Cockett et al., 2015). The final model was evaluated by computing the residual between the observed and predicted data (Figs. 9 A and B, respectively), yielding a root mean square error (RMSE) of 0.01 mGal, as shown in Fig. 9C.

To better visualize the density distribution, three cross-sections were selected: two north-south (S—N) profiles and one west-east (W-E) profile matching the ground survey data points (dashed lines in Fig. 9). This allows for a clearer interpretation of subsurface density variations and structural features. The first profile, located on the eastern edge of the pluton (Fig. 10A), parallel to the y-axis, represents an area where the

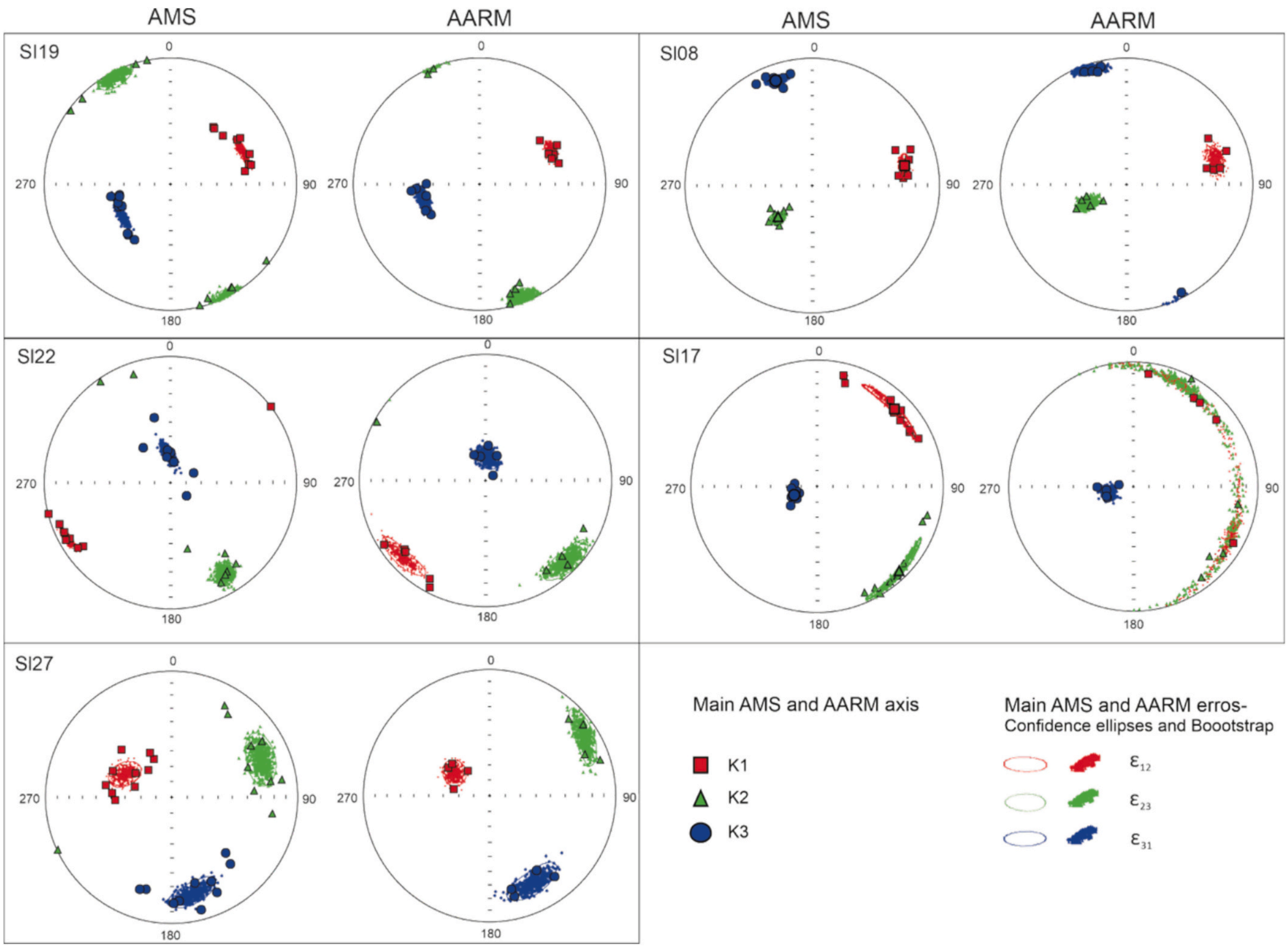

Fig. 7. Comparison of AARM and AMS directions for sites SI19, SI08, SI22, SI17 and SI27. While AMS is the bulk magnetic response of all minerals (dia, para, and ferromagnetic), the AARM isolates the ferromagnetic response and, in this case, is almost exclusively controlled by the shape anisotropy of MD magnetite (all sites have this behavior).

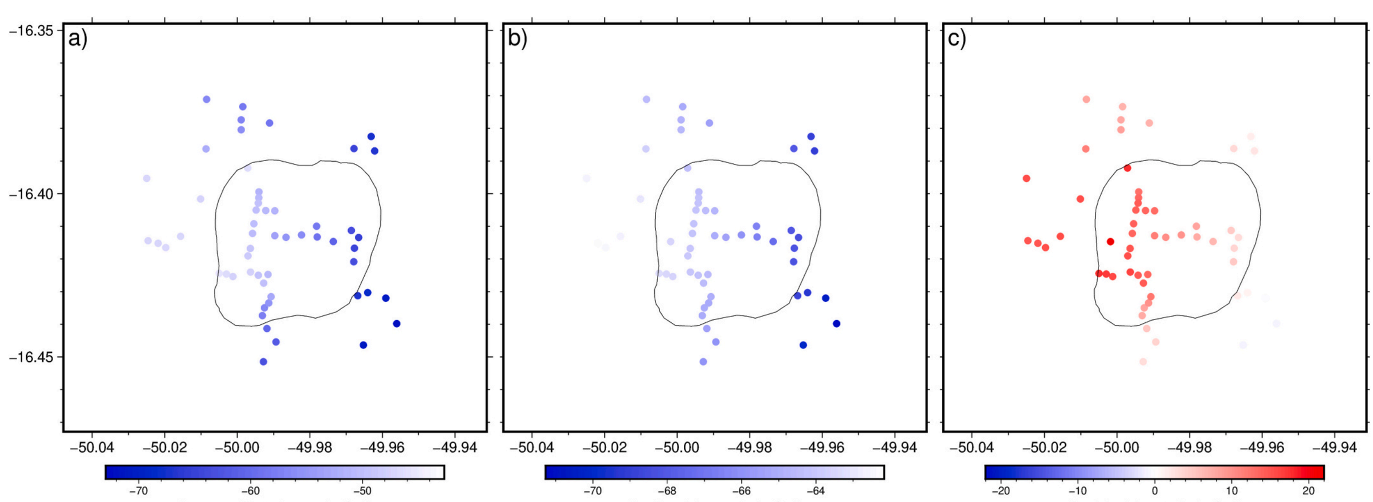

Fig. 8. The regional-residual separation process. The Bouguer disturbance (a) is decomposed into its deeper, regional component (b) and its shallower, residual component (c). The points represent the locations of ground survey stations, hued according to the intensity of the corresponding gravity field data. The solid black line corresponds to the pluton's boundary.

pluton has minimal thickness, and the density variation is less pronounced. In this region, diorite likely predominates. However, due to

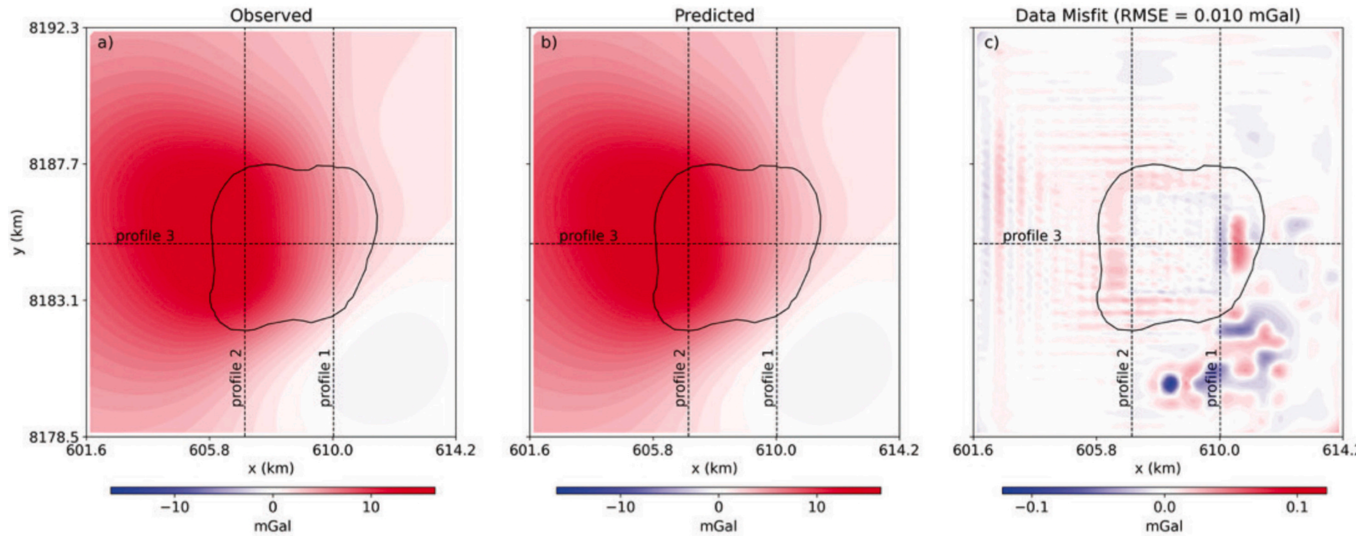

Fig. 9. Comparison of the observed and modeled gravity data. (a) Observed residual anomaly, (b) modeled prediction, and (c) Data misfit, highlighting the difference of an order of magnitude between observed and modeled data. The latter is given by the low value of the RMSE. The solid black line marks the pluton boundary, while the dashed lines represent the profiles analyzed.

the resolution of the model, it was not possible to discretize this influence with precision. The second profile (Fig. 10B), also parallel to the y-axis, shows that the pluton reaches greater depths. However, the model appears diffuse regarding the vertical boundary of the body, with the boundary potentially occurring between 2.5 and 4.5 km. This is a feature related to the smoothness caused by the regularization of the model, which leads to uncertainty in defining the exact depth of the body in this region. Finally, the third profile (Fig. 10C), parallel to the x-axis, demonstrates that the body dips to the west. This is further observed in the westward displacement of the positive peak of the residual anomaly (Fig. 9A). The westward dipping trend may be related to the structural setting of the intrusion zone, which occurs near a regional fault between the two enclosing units.

5. Discussion

5.1. Significance of magnetic fabric and gravity modeling

The CS is characterized by the presence of coarse-grained, multidomain (MD) magnetite, which plays a central role in controlling its magnetic fabric. This is evident from the susceptibility versus temperature (K-T) diagrams and further corroborated by both anisotropy of magnetic susceptibility (AMS) and anisotropy of anhysteretic remanent magnetization (AARM) measurements. The AARM ellipsoids, obtained within a low-coercivity window of 0 to 50 mT, confirm the dominance of MD/PSD magnetite grains in defining the magnetic fabric, as seen in other studies (Trindade et al., 2001; Temporim et al., 2020; Bellon et al., 2021). Similar to observations in other geological settings, the presence of MD magnetite in the CS is crucial for AMS studies, providing insights into the magmatic flow and foliation due to its control by magnetostatic energy rather than magnetocrystalline anisotropy (Dunlop and Ozdemir, 1997).

Although the magnetic lineation does not display a well-defined pattern, the magnetic foliations of both lithotypes within the pluton exhibit a distinct concentric arrangement centered on the gabbronorite core (Fig. 6). In the interior of the pluton, magmatic deformation is evident (Fig. 4). In the border of the pluton, including the diorite with mingling texture, the AMS patterns capture deformation imprinted by the magmas during their emplacement and crystallization. The diorite typically displays planar fabric with high P values (up to 1.332). The mafic core shows similar AMS patterns, characterized by planar fabric and high P values (up to 1.400). Additionally, at the border of the CS (diorite lithology), solid-state deformation occurs as feldspar recrystallized and aggregates of relatively small new grains between large old grains with undulose extinction (Fig. 4F). The undolose extinction in plagioclase may be associated with low-grade metamorphic conditions acting on intracrystalline deformation (Passchier and Trouw, 2006).

A clearer distinction emerges when microstructures are considered in detail. Plagioclase deformation twins, although classically associated with temperature above 400 °C (Passchier and Trouw, 2006) with high-temperature solid-state deformation, have been widely reported in partially crystallized mushes where residual melt allows crystal interaction during late stages of solidification (Vernon, 2018; Bouchez et al., 1992; Cavalcante et al., 2021; Nédélec and Bouchez, 2015). Their presence in the CS therefore supports intracrystalline deformation within a crystal-rich magma, complementing the AMS evidence of *syn*-magmatic fabrics. Bulging (BLG) recrystallization observed in feldspars represents a transition of low to medium temperature subsolidus deformation (~ 400 °C, Passchier and Trouw, 2006). Instead, BLG may develop during pluton exhumation or cooling, particularly along the margins where thermal gradients are steeper (Passchier and Trouw, 2006; Vernon, 2018; Stipp et al., 2002). In the CS, BLG textures likely developed during post-magmatic cooling and/or subsequent tectonic deformation, indicating that solid-state deformation overprinted the earlier magmatic fabric. Together, these microstructural criteria document a progressive overprint from syn-magmatic to subsolidus conditions, bridging the gap between magmatic fabrics and later modifications.

The bulk magnetic susceptibility of the specimens (k) varies widely across the CS (Fig. 11A). The lowest values are concentrated in the central and southern portions of the CS and locally in the northern and western portions. In contrast, the highest values are distributed in the northern, southeastern, and eastern portions. The distribution of bulk magnetic susceptibility values is not correlated with the lithotypes of the CS. The shape of the ellipsoids (T) also cannot be directly related to the pluton units. However, the highest "T" values are concentrated in the northern portion of the CS, while the lowest values are concentrated in the southern portion (Fig. 11B). The degree of anisotropy (P) exhibits significant variation. Fig. 11C shows a NE-SW direction strip of high anisotropic degree oriented in the NE-SW direction, which coincides with oblate ellipsoids, as shown in Fig. 11B. The southern and southeastern portions of the CS generally exhibit lower degrees of anisotropy,

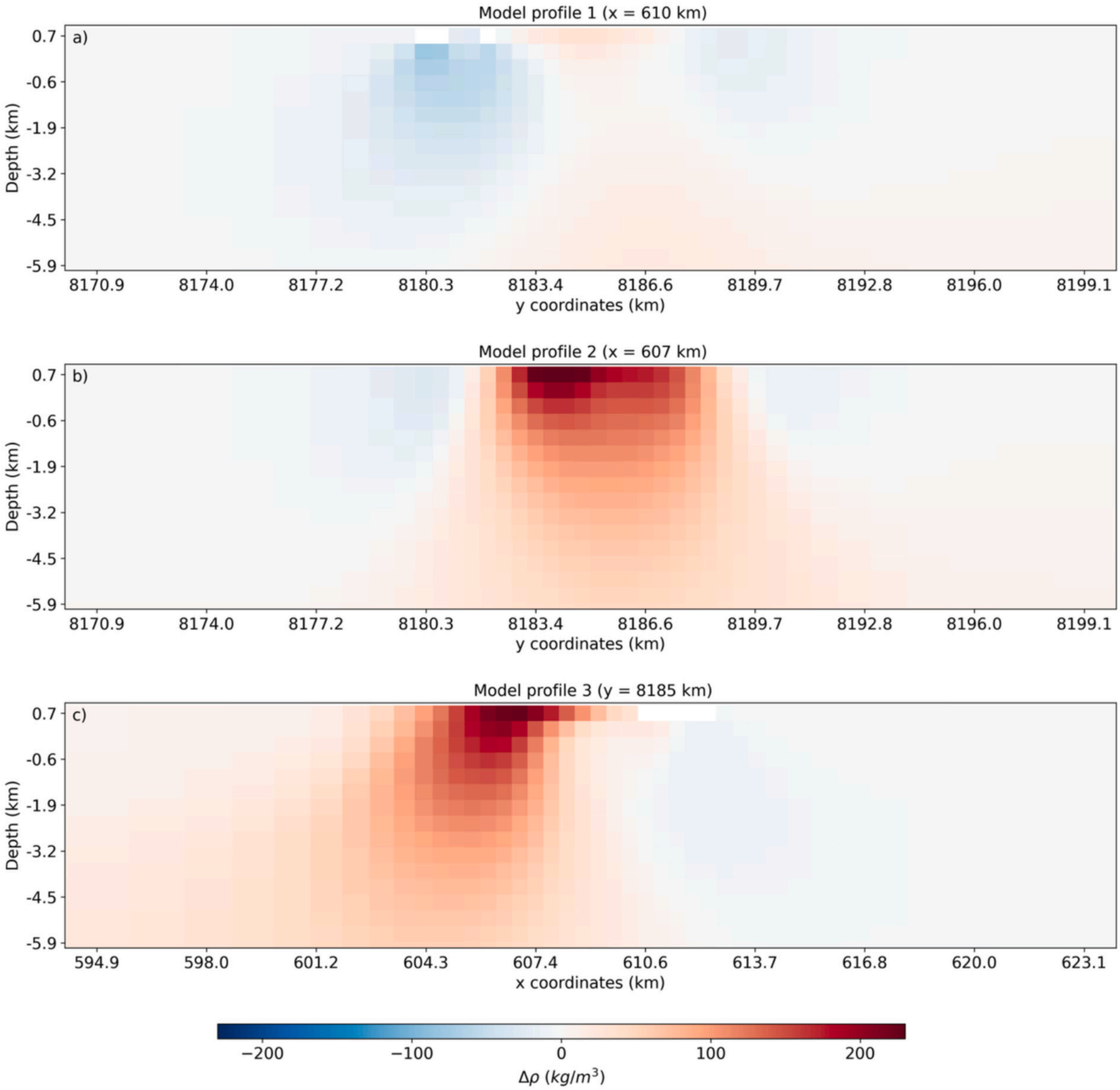

Fig. 10. Cross-sections of the pluton showing subsurface density variations. (a) Eastern border profile (S—N) showing this area pluton has minimal thickness. (b) Western border profile (S—N) with a diffuse vertical boundary, suggesting uncertainty in the exact depth of the pluton. (c) Middle section (W-E), showing the westward dip of the pluton.

which are predominantly associated with prolate ellipsoids. These features, represented by oblate and prolate ellipsoid shapes, cannot be directly attributed to any specific unit within the CS. However, it is evident that the northern portion of the CS displays a higher degree of anisotropy and a predominance of oblate ellipsoids, while the southern portion shows a lower degree of anisotropy and a predominance of prolate ellipsoids.

Although magmatic microtextures and microstructures are more abundant within the CS, the new AMS data show a strong anisotropic pattern also corroborated by the presence of a solid-state fabric (Fig. 4F). Therefore, the good agreement between magnetic and petrofabric geometries has been demonstrated by comparison of AMS and thin-section image analysis data (Fig. 4), confirming the utility of AMS in detecting cryptic structures in plutonic rocks. Syntectonic plutons are characterized by coherent, unidirectional magnetic lineations at the pluton scale (e.g., Archanjo et al., 2002; Bouchez et al., 1990; Langille et al., 2014). In contrast, the CS shows a well-defined concentric pattern of magnetic lineations, suggesting that magma deformation was controlled by magma buoyancy forces (Bellon et al., 2021; Oliveira et al., 2010; Sant'Ovaia et al., 2000; Temporim et al., 2020). However, the gravity inversion results add an additional dimension to this interpretation. The 3D modeling of residual anomalies reveals a westward-dipping geometry with thickened roots to the west, which directly complements the concentric magnetic fabrics observed in map view. This asymmetry indicates that while magma ascent was indeed buoyancy-driven, the final geometry of the body was strongly conditioned by crustal-scale shear zones at the Arenópolis–Anápolis–Itauçu boundary.

Thus, the integration of magnetic fabrics and gravimetric modeling demonstrates that the concentric magnetic foliation records magma flow organized around the gabbroic core within an asymmetric westward-dipping tabular intrusion, rather than lateral spreading within a radially symmetric pluton. The westward tilt of the pluton at depth likely reflects tectonic inheritance and the influence of regional crustal-scale structures during emplacement. When combined with the microstructural record, these results indicate a progressive sequence from *syn*-magmatic deformation (plagioclase twins) to localized subsolidus

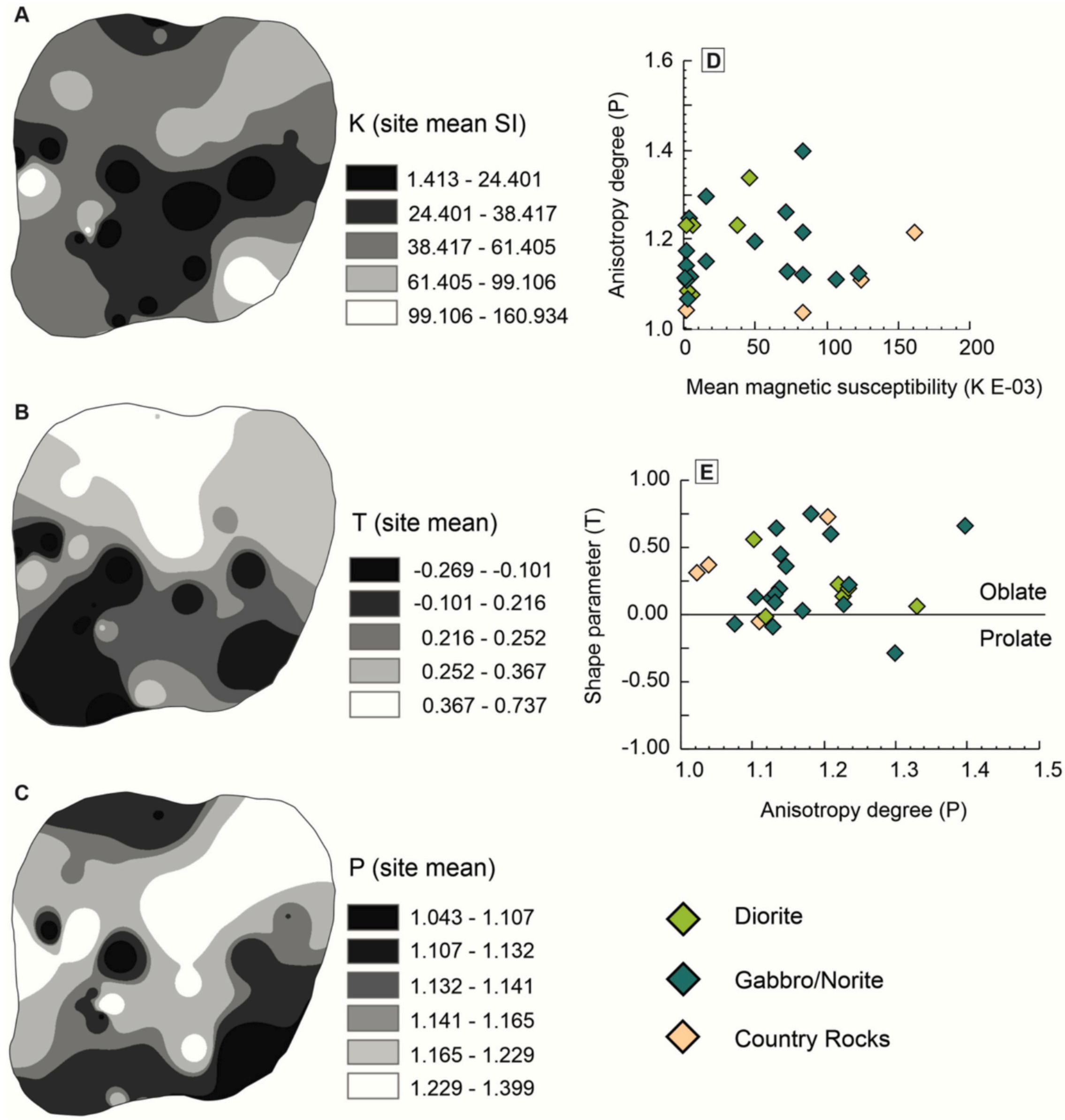

Fig. 11. Scalar magnetic parameters calculated through AMS data. Interpolation through minimum curvature of (A) bulk magnetic susceptibility (K), (B) shape parameters (T), (C) anisotropy degree (P) throughout the pluton. D) P vs K per site, showing a widespread susceptibility. E) P vs T per site, showing a wide variability of the data, with predominance of oblate ellipsoids.

overprint (BLG), a pattern also described in other post-collisional plutons worldwide (e.g., Archanjo et al., 2002; Barbey et al., 2008). Comparable cases of asymmetric plutons constrained by AMS and gravity data have been reported in other orogenic settings (Améglio and Vigneresse, 1999; Haederle and Atherton, 2002; Souza Junior et al., 2021), reinforcing the broader applicability of this integrated methodology.

In summary, the magnetic fabric reveals the internal organization of magma flow within the intrusion, while gravity data provide the large-scale framework of pluton asymmetry and depth distribution. Together, these datasets indicate that the CS pluton was emplaced incrementally within a structurally controlled, westward-dipping tabular system. In this context, the concentric magnetic fabrics likely reflect internally organized magma flow and incremental inflation within the intrusion, whereas the overall pluton geometry was controlled by inherited crustal discontinuities.

5.2. Model of emplacement

The integration of field observations, microstructural analysis (Bellon et al., 2021; Temporim et al., 2020; Oliveira et al., 2010), AMS data (Gleizes et al., 2006; Sant'Ovaia et al., 2000; Žák et al., 2013), gravimetric surveys (Souza Junior et al., 2021; Fontoura et al., 2024), and geochronological constraints (620 ± 7 Ma, U—Pb zircon; Laux, 2004) provides a comprehensive framework for understanding the mechanisms that controlled the emplacement of the Córrego Seco (CS) pluton. This integrated approach allowed a refined perspective on post-collisional mafic-ultramafic plutonism and on the possible role of crustal-scale structures acting as conduits for magma emplacement along the margins of the Brasília Orogenic Belt.

The pluton lies adjacent to the boundary between the Arenópolis Magmatic Arc and the Anápolis–Itauçu Complex, a crustal-scale discontinuity defined by N-S-striking shear zone and complex folding (Fig. 2, 3C). We propose that these regional structures acted as preferential conduits for magma ascent and emplacement during a post-collisional extension associated with orogenic collapse. Major crustal lineaments such as deep fault zones, coincident with first-order geological contacts, likely focused magma transport and accumulation, as observed in other orogenic provinces (e.g., Grocott et al., 2009; Pitcher, 1979; Seymour et al., 2020). Earlier models invoked diapiric ascent or ballooning to explain the rounded to concentric pattern and inverse zoning of the CS pluton (Laux et al., 2005; Silva et al., 2011; Lacerda Filho et al., 2021). However, those hypotheses lacked detailed structural or geophysical constraints. The results from integration of AMS, AARM, microstructural data, and 3D gravity inversion presented here, indicate instead that emplacement was strongly guided by regional shear zones and discontinuities along the Arenópolis Arc–Anápolis–Itauçu Complex boundary. Gravimetric inversion resolves a westward-dipping body with thicker roots to the west, inconsistent with near-symmetrical geometry expected for diapiric ballooning. Within this broader context, Fig. 12 schematically illustrates how crustal rheology governs the differential accommodation of mafic and felsic magmas during post-collisional stages: mafic intrusions exploit inherited weaknesses in the lower–middle crust, whereas felsic magmas pound at shallower levels. As illustrated in Fig. 12 we, thus, suggest that the asymmetric geometry of the CS is not an isolated case, but rather part of a systematic rheological control on late- to post-collisional magma emplacement along the Brasilia Orogenic Belt.

The internal magnetic fabric, predominantly concentric, defined by AMS ellipsoids and corroborated by AARM data, reveals a magmatic flow pattern around the gabbroic core. Toward the margins, petrographic evidence of feldspar bulging recrystallization (BLG; Fig. 4F) shows local overprint of the primary magmatic fabric by solid-state deformation. Similar overprints of magmatic and subsolidus fabrics have been documented in other post-collisional plutons (e.g., Archanjo et al., 2002; Barbey et al., 2008; Benn et al., 1994), reflecting interplay between magma emplacement and regional tectonics. The spatial variability of bulk magnetic susceptibility and anisotropy degree (Fig. 11), with higher anisotropy adjacent to regional shear zones, support this interpretation, and suggest late strain localization during or after emplacement.

Gravity data provides additional constraints on pluton architecture. The 3D inversion of residual anomalies (Fig.s 9–10) reveals a westward dip of the body and thickness variations, with deeper roots on the western side. These features are consistent with the structural setting where the intrusion is located, a westward dipping shear zone developed at the contact between competent orthogneiss and ductile metavolcano-sedimentary sequences of Arenópolis Arc, close to major crustal-scale discontinuity. (Fig. 2). The schematic model in Fig. 12 summarizes how inherited lineaments and rheological layering conditioned ascent pathways and final geometry. Similar approaches combining structural observations and gravimetric modeling have effectively constrained pluton emplacement elsewhere (e.g., Améglio et al., 1997; Launeau and Cruden, 1998; Solgadi and Sawyer, 2008).

Inverse zoning (dioritic margins, gabbroic core), and pervasive mingling textures at contacts, indicate emplacement by multiple closely timed pulses. These pulses were coeval but not fully homogenized, leading to feldspar transfer between facies and enclave swarms with variable degrees of hybridization. Rapid solidification of the magma body likely inhibited complete homogenization of the mixed magmas, thereby preserving a “frozen” state of magmatic mingling (e.g., Baxter and Feely, 2002; Perugini et al., 2005).

Taken together, the structural, magnetic, petrographic, and gravity datasets indicate that the Córrego Seco Pluton was emplaced incrementally by multiple pulses of magma, guided by regional shear zones and fault systems at first-order structures close to the boundary between the Arenópolis Arc and the Anápolis–Itauçu Complex. The westward-dipping, asymmetric architecture resolved by gravity inversion reflects the combined effects of magma buoyancy and tectonic inheritance.

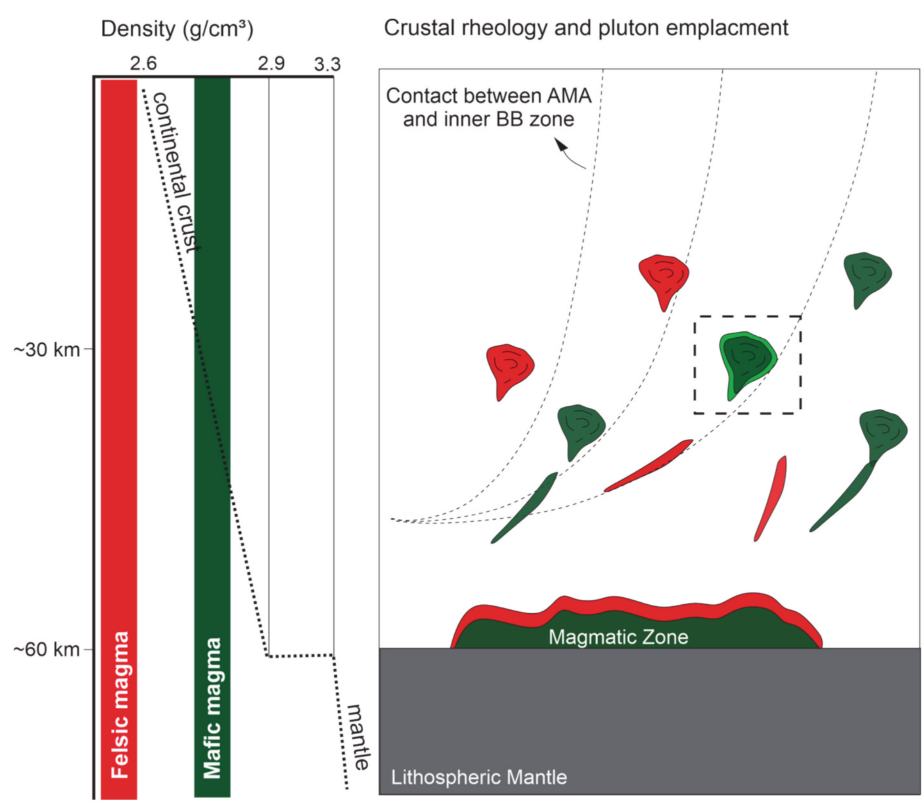

Fig. 12. Simplified scheme showing the emplacement of the post-collisional magmatism bodies according to the crustal rheology. AMA: Arenópolis Magmatic Arc. BOB: Brasília Orogenic Belt. The green portions represent the mafic magma and the red portions the felsic ones. Dashed lines in the figure on the right represent the contact between the AMA and the BB, as well as all additional parallel thrust faults. (For interpretation of the references to colour in this figure legend, the reader is referred to the web version of this article.)

Inverse zoning, mingling textures, and incomplete homogenization of coeval magmas point to a constructional history marked by repeated injections and rapid consolidation. This model, synthesized in Fig. 12, is consistent with other post-collisional plutons worldwide, where crustal discontinuities play the dominant role in focusing magma ascent and controlling final emplacement geometry (e.g., Bouchez et al., 1992; Archanjo et al., 2002; Solgadi and Sawyer, 2008; Martínez-Ardila et al., 2023). The timing of emplacement regarding the evolution of the orogen is believed to be late- to post-collisional, during an extensional phase, probably during the orogenic collapse of the BOB. Direct structural evidence for regional-scale extension or gravitational collapse in the study area remains limited. However, geochronological and geochemical characteristics of the post-collisional magmatism (including Corrego Seco pluton) (Silva et al., 2011; Augustin et al., 2023; Lacerda Filho et al., 2021; Carvalho et al., 2025) indicate that adiabatic decompression melting of the asthenosphere may have been triggered by a major tectonic disturbance, such as slab retreat or slab break-off. This interpretation is consistent with the regional review of the BOB (Pimentel et al., 2004), which proposed that between ~660 and 620 Ma the Arenópolis Arc underwent alternating extensional phases and episodes of slab tilting, producing intermittent back-arc extension and decompression melting within the arc system. Additional support for transient thermal weakening during this stage is provided by ultra-high-temperature (UHT) sapphirine-bearing paragneisses described in the high-grade rocks of the Anápolis–Itauçu Complex (e.g., Moraes et al., 2002; Baldwin and Brown, 2008). To explain these UHT conditions, Moraes et al. (2002) proposed tectonic models involving lithospheric thinning and partial collapse of the orogenic root through ductile necking or delamination processes.

Finally, the CS case underscores the broader utility of integrating AMS fabrics, microstructural analysis, and gravity modeling. Recent work on ultramafic intrusions shows that AMS is highly effective in capturing internal deformation and magma flow patterns, thereby providing robust constraints on emplacement histories (e.g. Austin et al., 2020; Martin et al., 2022). The approach adopted here is directly applicable to other mafic intrusions emplaced in convergent orogens, where transpressional regimes and inherited discontinuities govern magma ascent and accommodation.

5.3. Implications for the Brasília Orogenic Belt

The evolution of the Brasília Orogenic Belt provides the regional framework necessary to understand the emplacement of the Córrego Seco (CS) Pluton. Between ~800 and 630 Ma, the intra-oceanic Arenópolis Arc developed and were subsequently accreted to the western margin of the São Francisco–Congo craton (Pimentel et al., 2000a, 2000b; Pimentel et al., 2011). Progressive collision and crustal thickening were accompanied by granulite metamorphism in the Anápolis–Itauçu Complex between ~640 and 600 Ma (Piuzana et al., 2003; Martins et al., 2004; Quadros et al., 2021), marking the development of a hot, thickened lower crust.

In the aftermath of collision, mafic–ultramafic magmatism became widespread between ~630 and 590 Ma, recording the transition of late- to post-collisional tectonics. The CS pluton, dated at ~620 Ma (Laux, 2004), fits precisely into this magmatic pulse. Although direct P–T constraints are not available for the CS, geothermobarometric data from the nearby Mangabal Complex – a coeval and compositionally similar intrusion - indicate peak conditions of ~8.6 kbar and ~ 750 °C (Augustin and Della Giustina, 2019), equivalent to depths of ~28–30 km. The westward-dipping roots resolved by gravity inversion at the CS are consistent with this interpretation, suggesting that both intrusions were emplaced at mid- to lower-crustal levels under strong structural control.

Recent work on the Mangabal Complex further reveals that asthenospheric mantle melts contributed to the generation of layered mafic–ultramafic intrusions in the BOB (Augustin et al., 2023), while studies of the Americano do Brasil Complex highlight similar features of incremental emplacement along inherited shear zones (Augustin et al., 2025). Together, these intrusions define a regional suite of post-collisional mafic–ultramafic bodies assembled between ~630 and 590 Ma in association with major tectonic discontinuities (Fig. 2A).

In this space–time framework, the CS pluton exemplifies how inherited structural fabrics at the boundary between the Arenópolis Arc and the Anápolis–Itauçu Complex localized magma ascent, while deeper mantle inputs provided the thermal and compositional drivers of mafic magmatism. Its incremental assembly, inverse zoning, and asymmetric geometry are therefore not isolated features, but part of a systematic pattern of post-collisional mafic plutonism in the BOB during the terminal stages of Gondwana amalgamation.

6. Conclusions

The Córrego Seco (CS) Pluton provides a well-constrained example of post-collisional mafic magmatism emplaced along the structural boundary between the Arenópolis Arc and the Anápolis–Itauçu Complex during the late evolution of the Brasília Orogenic Belt. By integrating geological mapping, AMS and AARM analyses, microstructural investigation, and 3D gravity inversion, this study establishes an emplacement model that links internal magmatic fabrics with crustal-scale tectonic inheritance.

The pluton exhibits inverse zoning, with a gabbroic core surrounded by dioritic margins, and records incremental assembly through multiple magma pulses. Magnetic fabrics define a broadly concentric pattern around the mafic core, while gravity inversion reveals a westward-dipping tabular geometry with thickened roots toward the west. Together, these datasets indicate that magma emplacement was strongly controlled by inherited crustal discontinuities, with magnetic foliations recording magma flow and internal organization within an asymmetric intrusion geometry.

Microstructural evidence documents a progressive evolution from *syn*-magmatic deformation to localized subsolidus overprint along pluton margins, linking magmatic fabrics to late-stage solid-state deformation. The strong agreement between AMS and AARM fabrics further demonstrates that multidomain magnetite reliably records the internal fabric of the intrusion.

Collectively, these results indicate that the CS Pluton was emplaced within a tectonically structured crust, where inherited lithospheric anisotropies exerted a primary control on magma ascent pathways and final pluton architecture. Rather than representing a simple symmetric diapiric body, the intrusion records the combined influence of magma dynamics and regional structural inheritance during the terminal stages of the Brasília Orogenic Belt evolution.

Beyond its local significance, the Córrego Seco Pluton provides a rare example in which magnetic fabrics, microstructural observations, and 3D gravity modeling converge toward a consistent emplacement model. The integrated dataset reveals that an apparently isotropic post-collisional intrusion may preserve a well-organized internal architecture linked to crustal-scale structural inheritance. By documenting the geometry, internal fabric development, and emplacement history of the pluton, this study contributes new constraints on how mafic magmas are assembled and organized along major lithospheric discontinuities during the late stages of orogenic evolution. These results also provide a framework for interpreting other Ediacaran mafic intrusions emplaced along the Arenópolis Arc and elsewhere in the Brasília Belt.

Data and code availability

The Python source code used to produce the gravity models results is available at https://github.com/Souza-junior/Gravity_CS under the MIT open-source license.

We used all open-source packages in the Jupyter Notebook programming environment (Kluyver et al., 2016). We performed coordinate manipulations, generated regular grids, and performed data interpolation with the aid of Verde (Uieda, 2018). Boule package (Uieda and Soler, 2020a) for calculation of the normal gravity. The Harmonica package (Fatiando a Terra Project et al., 2023) was used in the terrain gravity effects correction and also for the equivalent layer technique. The orthometric and geoid models were acquired from the GMT database (Wessel et al., 2019), and the map generation was handled by the PyGMT package (Uieda et al., 2021). The inversion of gravity data was conducted using the SimPEG software (Cockett et al., 2015).

CRediT authorship contribution statement

F.A. Temporim: Writing – original draft, Validation, Supervision, Resources, Project administration, Methodology, Investigation, Funding acquisition, Formal analysis, Data curation, Conceptualization. **G.S. Costa:** Writing – review & editing, Validation, Software, Methodology, Investigation. **G.F. Souza-Junior:** Writing – review & editing, Visualization, Validation, Software, Investigation, Formal analysis. **R.P. Melo:** Writing – original draft, Supervision, Resources, Project administration, Methodology, Funding acquisition, Formal analysis, Data curation, Conceptualization. **L.M. Barros:** Writing – review & editing, Software, Methodology, Investigation. **S.W.O. Rodrigues:** Writing – original draft, Supervision, Methodology, Investigation, Formal analysis, Data curation. **D.E. Cavalcanti:** Writing – review & editing, Supervision, Methodology, Investigation, Formal analysis, Data curation. **M.A. Reis:** Writing – review & editing, Validation, Investigation. **J.M.S. Carneiro:** Writing – review & editing, Methodology, Investigation, Data curation. **J.A.S. Fontoura:** Writing – review & editing, Investigation. **R.I.F. Trindade:** Writing – review & editing, Validation.

Declaration of competing interest

The authors declare that they have no known competing financial interests or personal relationships that could have appeared to influence the work reported in this paper.

Acknowledgements

The authors would like to express their gratitude to Edriane B. for her support in the acquisition of data during fieldwork. The National Observatory (ON) for lending the gravimeter for data acquisition. The image Processing and Geoprocessing Laboratory (LAPIG) for lending the Differential Global Positioning System. The infrastructure and collaborations of the Laboratório de Paleomagnetismo of the Universidade de São Paulo. This work was funded by grant from the National Council for Scientific and Technological Development (CNPq) (# 404058/2023-0). The authors gratefully acknowledge the constructive comments and suggestions provided by the three anonymous reviewers and the editor, which significantly improved the quality and clarity of this manuscript.

Appendix A. Supplementary data

Supplementary data to this article can be found online at https://doi.org/10.1016/j.tecto.2026.231299.

Data availability

Data will be made available on request.

References

Alkmim, F.F., Marshak, S., Pedrosa-Soares, A.C., Peres, G.G., Cruz, S.C.P., Whittington, A., 2006. Kinematic evolution of the Araçuaí–West Congo Orogen in Brazil and Africa: nutcracker tectonics during the Neoproterozoic assembly of Gondwana. Precambrian Res. 149, 43–64.

Almeida, F.F.M., 1967. Origem e evolução da plataforma brasileira. Bol. Div. Geol. Mineral. 241, 36. Rio de Janeiro.

Almeida, F.F.M., 1968. Evolução tectônica do centro-oeste brasileiro no proterozóico superior. Anais Acad. Brasil. Ciências 40, 285–295.

Almeida, F.F.M., Hasui, Y., Brito Neves, B.B., Fuck, R.A., 1981. Brazilian structural provinces: an introduction. Earth Sci. Rev. 17, 1–29. https://doi.org/10.1016/0012-8252(81)90003-9.

Améglio, L., Vigneresse, J.L., 1999. Geophysical imaging of the shape of granitic intrusions at depth: a review. Geol. Soc. Spec. Publ. 168 (1), 39–54. https://doi.org/10.1144/GSL.SP.1999.168.01.04.

Améglio, L., Vigneresse, J.L., Bouchez, J.L., 1997. Granite pluton geometry and emplacement mode inferred from combined fabric and gravity data. In: Granite: From Segregation of Melt to Emplacement Fabrics, 8. Springer, Dordrecht, pp. 199–214. https://doi.org/10.1007/978-94-017-1717-5_13.

Aranguren, A., Tubía, J.M., Bouchez, J.L., Vigneresse, J.L., 1996. The Guitiriz granite, Variscan belt of northern Spain: extension-controlled emplacement of magma during tectonic escape. Earth Planet. Sci. Lett. 139 (1–2), 165–176. https://doi.org/10.1016/0012-821X(95)00239-9.

Araújo, V.A., Oliveira, C.C., Camargo, M.A., Barreto Filho, J.A., Andrade, R.S., 1997. Programa Levantamentos Geológicos Básicos do Brasil: Folha Itaberaí (SE.22-X-A-III), Goiás. CPRM, Goiânia 83.

Archanjo, C.J., Trindade, R.I., Bouchez, J.L., Ernesto, M., 2002. Granite fabrics and regional-scale strain partitioning in the Seridó belt (Borborema Province, NE Brazil). Tectonics 21 (1), 1–14. https://doi.org/10.1029/2000TC001269.

Augustin, C.T., Della Giustina, M.E.S., 2019. Geology and metamorphism of the neoproterozoic Mangabal complex: an example of Ni–Cu-PGE mineralizedintrusion in the Goiás Magmatic Arc, Central Brazil. J. S. Am. Earth Sci. 90, 504–519. https://doi.org/10.1016/j.jsames.2018.12.013.

Augustin, C.T., Mungall, J.E., Schutesky, M.E., Chamberlain, K.R., Ernst, R., Garcia, V.B., 2023. U-Pb in-situ SIMS baddeleyite and zircon dates and thermodynamic modeling of the Mangabal complex: Indications of asthenospheric mantle influence in the formation of layered intrusions of the Brasília orogen. Gondwana Res. 122, 93–111. https://doi.org/10.1016/j.gr.2023.06.007.

Augustin, C., Mungall, J.E., Schutesky, M.E., Ernst, R.E., Ferreira Filho, C.F., 2025. Metamorphism overprint in mafic-ultramafic cumulates in the Mangabal and Americano do Brasil Complexes, Brasília Belt, Brazil. J. Geol. Soc. 182, jgs2024–238. https://doi.org/10.1144/jgs2024-238.

Austin, J.R., Crawford, A.J., Brand, H.E.A., Aitken, A.R.A., Smithies, R.H., Barnes, S.J., 2020. Deciphering deformation in ultramafic intrusions via magnetic fabric (AMS) and palaeomagnetic studies, Savannah Ni-PGE camp, NW Australia. Tectonophysics 793, 228608. https://doi.org/10.1016/j.tecto.2020.228608.

Baldwin, J.A., Brown, M., 2008. Age and duration of ultrahigh-temperature metamorphism in the Anápolis–Itauçu Complex, Southern Brasília Belt, central Brazil: constraints from U–Pb geochronology, mineral rare earth element chemistry and trace-element thermometry. J. Metamorph. Geol. 26 (2), 213–233. https://doi.org/10.1111/j.1525-1314.2007.00759.x.

Barbey, P., Gasquet, D., Pin, C., Bourgeix, A.-L., 2008. Igneous banding, schlieren and mafic enclaves in calc-alkaline granites: the Budduso pluton (Sardinia). Lithos 104 (1–4), 147–163. https://doi.org/10.1016/j.lithos.2007.12.004.

Baxter, S., Feely, M., 2002. Magma mixing and mingling textures in granitoids: examples from the Galway granite, Connemara, Ireland. Mineral. Petrol. 76 (1), 63–74. https://doi.org/10.1007/s007100200032.

Bellon, U.D., D'Agrella-Filho, M.S., Temporim, F.A., Souza Junior, G.F., Soares, C.C.V., Amaral, C.A.D., Gouvea, L.P., Trindade, R.I.F., 2021. Building an inversely zoned post-orogenic intrusion in the Neoproterozoic-Cambrian Araçuaí orogen (Brazil). J. Struct. Geol. 149, 104401. https://doi.org/10.1016/j.jsg.2021.104401.

Benn, K., Paterson, S.R., Lund, S.P., 1994. Magmatic fabrics and pluton emplacement. In: Bouchez, J.L., Hutton, D.H.W., Stephens, W.E. (Eds.), Granite: From Segregation of Melt to Emplacement Fabrics. Kluwer Academic Publishers, Dordrecht, pp. 183–201.

Bonin, B., 2004. Do coeval mafic and felsic magmas in post-collisional to within-plate regimes necessarily imply two contrasting, mantle and crustal, sources? A review. Lithos 78, 1–24. https://doi.org/10.1016/j.lithos.2004.04.042.

Bouchez, J.L., 1997. Granite is never isotropic: An introduction to AMS studies of granitic rocks. In: Bouchez, J.L., Hutton, D.H.W., Stephens, W.E. (Eds.), Granite: From Segregation of Melt to Emplacement Fabrics. Kluwer Academic Publishers, Dordrecht, pp. 95–112. https://doi.org/10.1007/978-94-017-1717-5_6.

Bouchez, J.L., Delas, C., Gleizes, G., Nédélec, A., Cuney, M., 1992. Submagmatic microfractures in granites. Geology 20, 35–38.

Bouchez, J.L., Gleizes, G., Djouadi, T., Rochette, P., 1990. Microstructure and magnetic susceptibility applied to emplacement kinematics of granites: the example of the foix pluton (French pyrenees). Tectonophysics 184 (2), 157–171. https://doi.org/10.1016/0040-1951(90)90051-9.

Bouchez, J.L., Guillet, P., Chevalier, F., 1981. Structures d'écoulement liées à la mise en place du granite de Guérande (Loire-Atlantique, France). Bull. Soc. Géol. Fr. 23, 387–399.

Bouchez, J.-L., Nicolas, A., 2021. Principles of Rock Deformation and Tectonics. Oxford University Press, Oxford. https://doi.org/10.1093/oso/9780192843876.001.0001.

Carneiro, J.S.M., Fuck, R.A., Dantas, E.L., 2021. Arenópolis sequence, evolution of a marginal basin in the Neoproterozoic Goiás magmatic arc, central Brazil. J. South Am. Earth Sci. 106, 103033. https://doi.org/10.1016/j.jsames.2020.103033.

Cavalcante, C., Meira, V.T., Magalhães, N., Hollanda, M.H.B.M., Oliveira, E., 2021. The role of Ediacaran synkinematic anatectic rocks and the late-orogenic charnockitic rocks in the development of the hot Araçuaí belt. Precambrian 365, 106396. https://doi.org/10.1016/j.precamres.2021.106396.

Chiaradia, M., 2009. Adakite-like magmas from fractional crystallization and melting-assimilation of mafic lower crust (Eocene Macuchi arc, Western Cordillera, Ecuador). Chem. Geol. 265 (3–4), 468–487. https://doi.org/10.1016/j.chemgeo.2009.05.014.

Cockett, R., Kang, S., Heagy, L.J., Pidlisecky, A., Oldenburg, D.W., 2015. SimPEG: an open source framework for simulation and gradient based parameter estimation in geophysical applications. Comput. Geosci. 85, 142–154. https://doi.org/10.1016/j.cageo.2015.09.015.

Cordani, U.G., Brito-Neves, B.B., D'Agrella, M.S., 2003. From Rodinia to Gondwana: A review of the available evidence from South America. Gondwana Res. 6 (2), 275–283. https://doi.org/10.1016/S1342-937X(05)70976-X.

Cordani, U.G., Pimentel, M.M., Araújo, C.E.G., Basei, M.A.S., Fuck, R.A., Girardi, V.A.V., 2013. Was there an Ediacaran Clymene Ocean in Central South America. Am. J. Sci. 313 (6), 517–539. https://doi.org/10.2475/06.2013.01.

Cordeiro, P.F. de O., de Oliveira, C.G., 2017. The Goiás Massif: implications for a pre-Columbia 2.2–2.0 Ga continent-wide amalgamation cycle in Central Brazil. Precambrian Res. 298, 403–420. https://doi.org/10.1016/j.precamres.2017.06.021.

Cordeiro, P.F.O., Oliveira, A.L.A.M., Della Giustina, M.E.S., Pimentel, M.M., Fuck, R.A., Matteini, M., 2021. Evolution of the Mara Rosa Magmatic Arc, Central Brazil: implications from zircon U–Pb geochronology, whole-rock geochemistry and Sm–Nd isotopes. J. South Am. Earth Sci. 111, 103457. https://doi.org/10.1016/j.jsames.2021.103457.

Cruz, C., Sant'Ovaia, H., Raposo, M.I.B., Lourenço, J.M., Almeida, F., Noronha, F., 2021. Unraveling the emplacement history of a Portuguese post-tectonic Variscan pluton using magnetic fabrics and gravimetry. J. Struct. Geol. 153, 104470. https://doi.org/10.1016/j.jsg.2021.104470.

Dampney, C., 1969. The equivalent source technique. Geophysics 34 (1), 39–53. https://doi.org/10.1190/1.1439996.

Day, R., Fuller, M., Schmidt, V.A., 1977. Hysteresis properties of titanomagnetites: Grain-size and compositional dependence. Phys. Earth Planet. Inter. 13 (4), 260–267. https://doi.org/10.1016/0031-9201(77)90108-X.

Carvalho, D.R., Aguiar, I.M., Temporim, F.A., Melo, R.P., Yokoyama, E., Carnero, J.S.M., Santiago, R.M., 2025. A slab break-off model for mafic–ultramafic igneous rocks in the South Brasília Belt: Insights related to post-collisional magmatism. J. South Am. Earth Sci. 167, 105786. https://doi.org/10.1016/j.jsames.2025.105786.

Dias, P.H.A., Reis, H.L.S., Valeriano, C.M., Rodrigues, J.B., Silva, M.A., Leite, M.M., Matos, C.A., 2025. Revisiting the geological evolution of the Brasília orogenic belt (Central Brazil) through the integration of tectonic and provenance studies. Precambrian Res. 418, 107693. https://doi.org/10.1016/j.precamres.2025.107693.

Dowty, E., 1976. Crystal structure and crystal growth. I. The influence of internal structure on morphology. Am 61, 448–459.

Dunlop, D.J., Ozdemir, O., 1997. Rock Magnetism Fundamentals and Frontiers. In: Rock Magnetism. Cambridge University Press. https://doi.org/10.1017/cbo9780511612794.

Fatiando a Terra Project, Esteban, F.D., Li, L., Oliveira Jr., V.C., Pesce, A., Shea, N., Soler, S.R., Tankersley, M., Uieda, L., 2023. Harmonica v0.6.0: Forward modeling, inversion, and processing gravity and magnetic data. Zenodo. https://doi.org/10.5281/zenodo.7690145.

Fontoura, J.A.S., Bitencourt, M.F., Savian, J.F., Padilha, D.F., Cardoso, V.S., Tomé, C.R., Meneghini, C., dos Santos Aquino, R., Trindade, R.I.F., 2024. Restoring a syntectonic transtensional pluton by integrating structural geology, anisotropy of magnetic susceptibility, and gravimetric modelling. J. Struct. Geol. 179, 105016. https://doi.org/10.1016/j.jsg.2023.105016.

Fossen, H., Cavalcante, G.C.G., 2017. Shear zones – A review. Earth-Sci. Rev. 171, 434–455. https://doi.org/10.1016/j.earscirev.2017.05.002.

Fuck, R.A., 1994. A Faixa Brasília e a Compartimentação Tectônica na Província Tocantins. In: Simpósio De Geologia Do Centro Oeste, 4., 1994, Brasília. SBG, Brasília, pp. 184–187.

Fuck, R.A., Pimentel, M.M., Alvarenga, C.J.S., Dantas, E.L., 2017. The Northern Brasília Belt. In: Heilbron, M., Cordani, U.G., Alkmim, F.F. (Eds.), São Francisco Craton, Eastern Brazil: Tectonic Genealogy of a Miniature Continent. Regional Geology Reviews. Springer, Cham, pp. 205–220. https://doi.org/10.1007/978-3-319-01715-0_11.

Geosoft Inc, 2015. Oasis montaj Version 8.4 User Guide. Geosoft Inc, Toronto, Canada.

Gleizes, G., Crevon, G., asrat, A., Barbey, P., 2006. Structure, age and model of emplacement of the Hercynian Boederes-Louron Pluton (Central Pyrenees, France). Int. J. Earth Sci. 95 (6), 1039–1052. https://doi.org/10.1007/s00531-006-0088-4.

Grocott, J., Arevalo, C., Welkner, D., Cruden, A.R., 2009. Fault-assisted vertical pluton growth: coastal Cordillera, north Chilean Andes. J. Geol. Soc. Lond. 166 (2), 295–301. https://doi.org/10.1144/0016-76492007-165.

Gupta, H.K. (Ed.), 2021. Encyclopedia of Solid Earth Geophysics. Encyclopedia of Earth Sciences Series. Springer. https://doi.org/10.1007/978-3-030-58631-7.

Haederle, M., Atherton, M.P., 2002. Shape and intrusion style of the Coastal Batholith, Peru. Tectonophysics 345 (1–4), 17–28. https://doi.org/10.1016/S0040-1951(01)00204-9.

Hinze, W.J., 2003. Bouguer reduction density, why 2.67? Geophysics 68 (5), 1559–1560. https://doi.org/10.1190/1.1620629.

Hrouda, F., Jelínek, V., Zapletal, K., 1990. ANISOFT: Program Package for Statistical Evaluation of Anisotropy Data. AGICO, Brno, Czech Republic.

Hutton, D.H.W., 1988. Granite emplacement mechanisms and tectonic controls: inferences from deformation studies. Earth Environ. Sci. Trans. Royal Soc. Edinburgh 79 (2–3), 245–255. https://doi.org/10.1017/S0263593300014255.

Ince, E.S., Barthelmes, F., Reißland, S., Elger, K., Förste, C., Flechtner, F., Schuh, H., 2019. ICGEM – 15 years of successful collection and distribution of global gravitational models, associated services and future plans. Earth Syst. Sci. Data 11, 647–674. https://doi.org/10.5194/essd-11-647-2019.

Jelínek, V., 1978. Statistical processing of anisotropy of magnetic susceptibility measured on groups of specimens. Stud. Geophys. Geod. 22 (1), 50–62. https://doi.org/10.1007/BF01613632.

Kluyver, T., Ragan-Kelley, B., Pérez, F., Granger, B., Bussonnier, M., Frederic, J., Kelley, K., Hamrick, J., Grout, J., Corlay, S., Ivanov, P., Avila, D., Abdalla, S., Willing, C., 2016. Jupyter notebooks – A publishing format for reproducible computational workflows. In: Loizides, F., Schmidt, B. (Eds.), Positioning and Power in Academic Publishing: Players, Agents and Agendas. IOS Press, pp. 87–90.

Lacerda Filho, J.V., Gollmann, K., Santos, D.R.V., Martins, F.R., Souza, J.O., Carneiro, J.S.M., Meneghini, P.F.V., Hattingh, K., Silva, E.R., Eberhardt, D.B., 2021. Projeto oeste de Goiás. CPRM, Goiânia, 2021. Escala 1:250.000. (Programa Novas Fronteiras: Levantamento Geológico e potencial de Novas Fronteiras).

Langille, J.M., Jessup, M.J., Cottle, J., Ahmad, T., 2014. Kinematic and thermal studies of the Leo Pargil dome: implications for syn-convergent extension in the NW Indian Himalaya. Tectonics 33, 1766–1786. https://doi.org/10.1002/2014TC003593.

Laux, J.H., 2004. Evolução do Arco Magmático de Goiás com base em dados geocronológicos U-Pb e Sm-Nd. Instituto de Geociências, Universidade de Brasília - UnB, Brasília, p. 113. Thesis.

Laux, J.H., Pimentel, M.M., Dantas, E.L., Armstron, R., Junges, S.L., 2005. Two Neoproterozoic custal accretion events in the Brasília Belt, Central Brazil. J. S. Am. Earth Sci. 18 (2), 183–198. https://doi.org/10.1016/j.jsames.2004.09.003.

Laux, J.H., Pimentel, M.M., Gioia, S.M.C.L., Ferreira, V.P., 2010. The Anicuns-Itaberaí volcano-sedimentary sequence, Goiás magmatic arc: new geochemical and Nd-S isotopic data. Geochim. Bras. 24 (1), 13–28.

Li, X., Götze, H.J., 2001. Ellipsoid, geoid, gravity, geodesy, and geophysics. Geophysics 66 (6), 1660–1668. https://doi.org/10.1190/1.1487109.

Liègeois, J.P., 1998. Preface-some words on the post-collisional magmatism. Lithos 45, 15–17.

Lowrie, W., 1997. Fundamentals of Geophysics. Cambridge University Press.

Launeau, P., Cruden, A.R., 1998. Magmatic fabric acquisition mechanisms in a syenite: results of a combined anisotropy of magnetic susceptibility and image analysis study. J. Geophys. Res. 103 (B3), 5067–5089. https://doi.org/10.1029/97JB02670.

Marsh, B.D., 1982. On the mechanics of igneous diapirism, stoping, and zone melting. Am. J. Sci. 282, 808–855.

Martin, S.A., Kavanagh, J.L., Biggin, A.J., 2022. Deciphering syn- and post-emplacement processes in shallow mafic dykes using magnetic anisotropy. J. Volcanol. Geotherm. Res. 422, 107456. https://doi.org/10.1016/j.jvolgeores.2021.107456.

Martínez-Ardila, A.N., Pompe, L., Clausen, B.L., Paterson, S.R., Holk, G.J., Luffi, P., 2023. A synthesis of the Peruvian Coastal Batholith: an exploration of temporal histories, causes of compositional diversity, and tectonomagmatic links in arcs. Lithos 456–457, 107298. https://doi.org/10.1016/j.lithos.2023.107298.

Martins, J., Gonçalves, L., Fuck, R.A., Pimentel, M.M., 2004. Petrology, geochemistry and geochronology of granulites of the Anápolis–Itauçu Complex, central Brazil: Neoproterozoic lower crust in the Tocantins Province. Precambrian Res. 135, 133–157.

Molyneux, S.J., Hutton, D.H.W., 2000. Evidence for significant granite space creation by the ballooning mechanism: the example of the Ardara pluton, Ireland. GSA Bull. 112 (10), 1543–1558. https://doi.org/10.1130/0016-7606(2000)112<1543:EFSGSC>2.0.CO;2.

Moraes, R., Brown, M., Fuck, R.A., Camargo, M.A., Lima, T.M., 2002. Characterization and P-T evolution of melt-bearing ultrahigh-temperature granulites: an example from the anapolis-itaucu complex of the Brasilia Fold Belt. Brazil. J. Petrol. 43 (9), 1673–1705. https://doi.org/10.1093/petrology/43.9.1673.

Mota and Silva, J., 2009. O Complexo Máfico-ultramáfico Acamadado de Americano do Brasil e sua mineralização. de Ni-Cu-Co. M.Sc. Thesis, Universidade de Brasília, Brasília, pp. 101–pp.

Nagy, D., Papp, G., Benedek, J., 2000. The gravitational potential and its derivatives for the prism. J. Geod. 74, 552–560. https://doi.org/10.1007/s001900000116.

Nédélec, A., Bouchez, J.L., 2015. Granites: Petrology, Structure, Geological Setting and Metallogeny, first ed. Press, Oxford University, Oxford.

Nunes, N.S.V., 1990. Geologia e Potencial Mineral da Região de Anicuns, Goiás. Universidade de Brasília - UnB, Instituto de Geociências, p. 188. Thesis.

Oliveira, D.C., Neves, S.P., Trindade, R.I.F., Dall'Agnol, R., Mariano, G., Correia, P.B., 2010. Magnetic anisotropy of the Redenção granite, eastern Amazonian craton (Brazil): implications for the emplacement of A-type plutons. Tectonophysics 493 (1–2), 27–41. https://doi.org/10.1016/j.tecto.2010.07.018.

Oriolo, S., Oyhantçabal, P., Wemmer, K., Siegesmund, S., 2017. Contemporaneous assembly of Western Gondwana and final Rodinia break-up: Implications for the supercontinent cycle. Geosci. Front. 8 (6), 1431–1445. https://doi.org/10.1016/j.gsf.2017.01.009.

Passchier, C.W., Trouw, R.A., 2006. Microtectonics. Springer, p. 366.

Passo-Vieira, O., Melo, R.P., Fumes, R.A., Brod, G.S., Temporim, F.A., Rodrigues, S.W.O., Luvizotto, G.L., 2026. Tectonometamorphic evolution of the Anicuns-Itaberaí Sequence, Southern Brasília Orogen: evidence of deep burial and syn-collisional exhumation. J. S. Am. Earth Sci. 173, 105974. https://doi.org/10.1016/j.jsames.2026.105974.

Pašteka, R., Mikuška, J., Meurers, B., 2017. Chapter 1 - Introduction. In: Pašteka, R., Mikuška, J., Meurers, B. (Eds.), Understanding the Bouguer Anomaly. Elsevier, pp. 1–11. https://doi.org/10.1016/B978-0-12-812913-5.00011-7.

Paterson, S.R., Vernon, R.H., Tobisch, O.T., 1989. A review of criteria for the identification of magmatic and tectonic foliations in granitoids. J. Struct. Geol. 11 (3), 349–363. https://doi.org/10.1016/0191-8141(89)90074-6.

Paterson, S.R., Vernon, R.H., Tobisch, O.T., 1999. A review of criteria for the identification of magmatic and tectonic foliations in granitoids. J. Struct. Geol. 21, 1131–1146.

Patiño Douce, A.E., 1999. What do experiments tell us about the relative contributions of crust and mantle to the origin of granitic magmas? In: Castro, Fernández, Vigneresse (Eds.), Understanding Granites, 168. Geological Society, London, pp. 55–75. Special Publication.

Perugini, D., Poli, G., Valentini, L., 2005. Strange attractors in plagioclase oscillatory zoning: petrological implications. Contrib. Mineral. Petrol. 149 (4), 482–497. https://doi.org/10.1007/s00410-005-0667-6.

Philpotts, A.R., 1990. Principles of Igneous and Metamorphic Petrology. Prentice Hall, Englewood Cliffs, NJ.

Pimentel, M.M., 2016. The tectonic evolution of the Neoproterozoic Brasília Belt, central Brazil: a geochronological and isotopic approach. A evolução tectônica da Faixa Brasília, Brasilcentral: uma abordagem geocronológica e isotópica. Braz. J. Geol. 46 (1), 67–82. https://doi.org/10.1590/2317-4889201620150004.

Pimentel, M.M., Fuck, R.A., 1992. Neoproterozoic crustal accretion in central Brazil. Geology 20, 375–379. https://doi.org/10.1130/0091-7613(1992)020<0375:NCAICB>2.3.CO;2.

Pimentel, M.M., Fuck, R.A., Alvarenga, C.J.S., 1996. Post-Brasiliano (Pan-African) high-K granitic magmatism in Central Brazil: the role of late Precambrian-early Palaeozoic extension. Precambrian Res. 80, 217–238. https://doi.org/10.1016/S0301-9268(96)00016-2.

Pimentel, M.M., Whitehouse, M.J., Viana, M.D.G., Fuck, R.A., Machado, N., 1997. The Mara Rosa Arc in the Tocantins Province: further evidence for Neoproterozoic crustal accretion in Central Brazil. Precambrian Res. 81 (3–4), 299–310. https://doi.org/10.1016/s0301-9268(96)00039-3.

Pimentel, M.M., Fuck, R.A., Gioia, S.M.C.L., 2000a. The neoproterozoic Goiás Magmatic Arc, Central Brazil: a review and new Sm-Nd isotopic data. Rev. Bras. Geocienc. 30 (1), 35–39. https://doi.org/10.25249/0375-7536.2000301035039.

Pimentel, M.M., Fuck, R.A., Jost, H., Ferreira Filho, C.F., Araújo, S.M., 2000b. The basement of the Brasília Belt and the Goiás Magmatic Arc. In: Cordani, et al. (Eds.), Tectonic Evolution of South America, 31st International Geological Congress, pp. 195–229.

Pimentel, M.M., Jost, H., Fuck, R.A., 2004. O embasamento da Faixa Brasília e o Arco Magmático de Goiás. In: Mantesso-Neto, V., Bartorelli, A., Carneiro, C.D.R., Brito Neves, B.B. (Eds.), Geologia do Continente Sul-Americano: Evolução da Obra de Fernando Flávio Marques de Almeida. Beca, São Paulo, pp. 355–368.

Pimentel, M.M., Rodrigues, J.B., Della Giustina, M.E.S., Junges, S., Matteini, M., Armstrong, R., 2011. The tectonic evolution of the Neoproterozoic Brasília Belt, Central Brazil: a geochronological and isotopic approach. J. S. Am. Earth Sci. 31, 397–409. https://doi.org/10.1016/j.jsames.2011.02.010.

Pitcher, W.S., 1979. The nature, ascent, and emplacement of granitic magrnas. J. Geol. Society London 163, 627–662. https://doi.org/10.1144/gsjgs.136.6.0627.

Piuzana, D., Pimentel, M.M., Fuck, R.A., Armstrong, R., 2003. SHRIMP U-Pb and Sm-Nd data for the Araxá Group and associated magmatic rocks: constraints for the age of sediments and geodynamic context of the southern Brasília Belt, Central Brazil. Precambrian Res. 125 (1–2), 139–160. https://doi.org/10.1016/S0301-9268(03)00107-4.

Quadros, A.M., Schmitt, R.S., et al., 2021. Age and duration of ultrahigh-temperature metamorphism in the Anápolis–Itauçu Complex. J. Metamorph. Geol. 39, 1003–1026. https://doi.org/10.1111/jmg.12603.

Rochette, P., 1987. Magnetic susceptibility of the rock matrix related to magnetic fabric studies. J. Struct. Geol. 9 (8), 1015–1020. https://doi.org/10.1016/0191-8141(87)90009-5.

Sant'Ovaia, H., Bouchez, J.L., Noronha, F., Leblanc, D., Vigneresse, J.L., 2000. Composite-laccolith emplacement of the post-tectonic Vila Pouca de Aguiar granite pluton (northern Portugal): a combined AMS and gravity study: transactions of the Royal Society of Edinburgh. Earth Sci. Earth Environ. Sci. Trans. R. Soc. Edinb. 91 (1–2), 123–137. https://doi.org/10.1017/S026359330000732X.

Seymour, N.M., Singleton, J.S., Mavor, S.P., Gomila, R., Stockli, D.F., Heuser, G., Arancibia, G., 2020. The relationship between magmatism and deformation along the intra-arc strike-slip Atacama fault system, northern Chile. Tectonics 39, e2019TC005702. https://doi.org/10.1029/2019TC005702.

Silva, J., Ferreira Filho, C.F., Bunh, B., Dantas, E.L., 2011. Geology, petrology and geochemistry of the Americano do Brasil layered intrusion, Central Brazil, and its Ni Cu sulfide deposits. Mineral. Deposita 46, 57–90. https://doi.org/10.1007/s00126-010-0312-9.

Soler, R.S., Uieda, L., 2020. A Better Strategy for Interpolating Gravity and Magnetic Data. In: EGU General Assembly Conference Abstracts, p. 549. https://doi.org/10.5194/egusphere-egu2020-549.

Solgadi, F., Sawyer, E.W., 2008. Formation of diapirs in a syntectonic environment: AMS and structural evidence. Tectonophysics 464, 246–262.

Souza Junior, G.F., Trindade, R.I.F., Temporim, F.A., Bellon, U.D., Gouvêa, L.P., Soares, C.C., Amaral, C.A.D., Louro, V.H.A., 2021. Imaging the roots of a post-collisional pluton: implications for the voluminous Cambrian magmatism in the Araçuaí Orogen, Brazil. Tectonophysics 821, 229146. https://doi.org/10.1016/j.tecto.2021.229146.

Stipp, M., Stünitz, H., Heilbronner, R., Schmid, S.M., 2002. The eastern Tonale fault zone: a "natural laboratory" for crystal plastic deformation of quartz over a temperature range from 250 to 700 °C. J. Struct. Geol. 24 (12), 1861–1884. https://doi.org/10.1016/S0191-8141(02)00035-4.

Telford, W.M., Geldart, L.P., Sheriff, R.E., 1990. Applied Geophysics, 2nd ed. Cambridge University Press.

Temporim, F.A., Trindade, R.I.F., Tohver, E., Soares, C.C., Gouvea, L.P., Egydio-Silva, M., Amaral, C.A.D., Souza Junior, G.F., 2020. Magnetic fabric and geochronology of a Cambrian "isotropic" pluton in the Neoproterozoic Araçuaí Orogen. Tectonics 39 (6). https://doi.org/10.1029/2019TC005877.

Trindade, R.I.F., Bouchez, J.L., Bolle, O., Nédélec, A., Peschler, A., Poitrasson, F., 2001. Secondary fabrics revealed by remanence anisotropy: methodological analysis and examples from plutonic rocks. Geophys. J. Int. 147 (2), 310–318. https://doi.org/10.1046/j.0956-540x.2001.01529.x.

Uhlein, A., Fonseca, M.A., Seer, H.J., Dardenne, M.A., 2012. Tectônica da Faixa de Dobramentos Brasília – Setores Setentrional e Meridional. Geonomos 20 (2), 1–14. https://doi.org/10.18285/geonomos.v2i20.243.

Uieda, L., 2018. Verde: Processing and gridding spatial data using Green's functions. J. Open Source Softw. 3 (29), 957. https://doi.org/10.21105/joss.00957.

Uieda, L., Soler, S., 2020a. Boule v0.2.0: Reference Ellipsoids for Geodesy, Geophysics, and Coordinate Calculations. Zenodo. https://doi.org/10.5281/zenodo.3939204.

Uieda, L., Soler, S., 2020b. Evaluating the accuracy of equivalent-source predictions using cross-validation. In: EGU General Assembly Conference Abstracts, p. 15729. https://doi.org/10.5194/egusphere-egu2020-15729.

Uieda, L., Tian, D., Leong, W.J., Toney, L., Schlitzer, W., Grund, M., Newton, T., Ziebarth, M., Jones, M., Wessel, P., 2021. PyGMT: A Python interface for the Generic Mapping Tools. Zenodo. https://doi.org/10.5281/zenodo.4522136.

Valeriano, C.M., Pimentel, M.M., Heilbron, M., Almeida, J.C.H., Trouw, R.A.J., 2008. Tectonic evolution of the Brasília belt, Central Brazil, and early assembly of Gondwana. In: Pankhurst, R.J., Trouw, R.A.J., Brito Neves, B.B., De Wit, M.J. (Eds.), West Gondwana: Pre- Cenozoic Correlations across the South Atlantic Region. Geological Society, London, pp. 197–210. Special Publications, 294.

Vernon, R.H., 2018. Practical Guide to Rock Microstructures. Cambridge Press, p. 443.

Viana, M.D.G., Pimentel, M.M., Whitehouse, M.J., Fuck, R.A., Machado, N., 1995. O Arco Magmático De Mara Rosa, Goiás: Geoquímica E Geocronologia E Suas Implicações Regionais. Rev. Brasil. Geoci. 25 (2), 111–123. https://doi.org/10.25249/0375-7536.1995111123.

Vigneresse, J.L., Tikoff, B., Améglio, L., 1999. Modification of the regional stress field by magma intrusion and formation of tabular granitic plutons. Tectonophysics 302 (3–4), 203–224. https://doi.org/10.1016/S0040-1951(98)00285-6.

Wessel, P., Luis, J.F., Uieda, L., Scharroo, R., Wobbe, F., Smith, W.H.F., Tian, D., 2019. The generic mapping tools version 6. Geochem. Geophys. Geosyst. 20 (11), 5556–5564. https://doi.org/10.1029/2019GC008515.

Wilson, M., 2012. Igneous Petrogenesis: A Global Tectonic Approach. Springer.

Wojtal, S., Blenkinsop, T., Tikoff, B., 2022. An Integrated Framework for Structural Geology: Kinematics, Dynamics, and Rheology of Deformed Rocks. John Wiley & Sons, Hoboken.

Woodcock, N.H., 1977. Specification of fabric shapes using eigenvalue methods. Geol. Soc. Am. Bull. 88, 1231–1236.

Žák, J., Verner, K., Sláma, J., Kachlík, V., Chlupáčová, M., 2013. Multistage magma emplacement and progressive strain accumulation in the shallow-level Krkonoše-Jizera plutonic complex, Bohemian Massif. Tectonics 32, 1493–1512. https://doi.org/10.1002/tect.20088.